49th AIAA Aerospace Sciences Meeting including the New Horizons Forum and Aerospace Exposition
4 - 7 January 2011, Orlando, Florida
AIAA 2011-774

Efficient Solutions of the Euler Equations in a Time-Adaptive Space-Time Framework

Karthik Mani * and Dimitri J. Mavriplis †

Department of Mechanical Engineering, University of Wyoming, Laramie, Wyoming 82071-3295

The inviscid Euler equations are solved using a space-time finite-volume discretization. The method inherently accounts for deforming computational meshes. Traditional implicit unsteady discretizations rely on solving the spatial problem with appropriate temporal terms added in an implicit sense at each time level while advancing forward in time one time-step at a time. The approach in this paper is to unify both time and space dimensions and operate on a single computational mesh that spans both the spatial and temporal domains of interest. In essence all unknowns at all spatial and temporal locations in the domain of interest are solved implicitly in one shot. The primary advantage of this approach is the spatially non-uniform variation of the time-step size. The goal is to reduce the total degrees-of-freedom by requiring that only certain spatial locations advance with high resolution in time. The adjoint weighted residual method is used to identify regions in the space-time domain that require higher temporal resolution, thus targeting only certain spatial locations that have to be advanced slowly in time while maintaining overall solution accuracy. Both the reduction of the total unknowns in the solution and the faster convergence due to implicit coupling in time combine to form a efficient unsteady solver. The actual non-linear problem is solved using the Newton-Krylov preconditioned GMRES method with ILU(0) as the preconditioner. While the method converges rapidly, the memory requirements are high even for relatively small problems. This problem is alleviated by splitting the time domain into a limited number of slabs and solving for all unknowns within a slab implicitly while advancing in time slab-by-slab.

I. Introduction

The fundamental goal of numerical simulations is to obtain accurate solutions to nonlinear governing equations at acceptable computational expense. In the early days of the field, unsteady problems were deemed unreasonably expensive and the focus remained on accurate solutions to steady-state problems. Several algorithmic advances in terms of numerically solving nonlinear equations have been made over the years to reduce the cost associated with obtaining accurate solutions.[1,2] Such advances coupled with improved hardware capabilities have since enabled solutions to unsteady problems, firstly using explicit methods and then progressing to faster and more efficient implicit time-integration schemes. While simple unsteady problems remain tractable, problems exhibiting strong unsteadiness currently require simulation times running into days or even weeks. Several methods have been been investigated to address this issue. Higher-order implicit time-integration schemes[3–7] operate directly in the time domain and maintain solution accuracy while using fewer time-steps. For problems exhibiting strong periodic behavior, frequency domain methods[8,9] transform the unsteady problem into time spectral space and restrict the number of modes required for the solution. Solution techniques such as multigrid[10–12] have also been developed to reduce the cost associated with solving the non-linear system of equations at each each time-step. Although frequency-domain based techniques are quite powerful, their performance is inefficient when applied to problems with no dominant periodicity. This necessitates the development of improved algorithms operating in the time domain so as to be applicable to all unsteady problems in a general sense.

In the context of implicit time-integration schemes, which impose no restrictions on the time-step size, additional savings can be realized by varying the time-step size at each implicit time-step provided an estimate of the local temporal error at each time-step is available. This approach is directly analogous to the universally common practice of utilizing non-uniform spatial meshes when solving problems. It is unnecessary to use high spatial resolution in regions of very low gradients such as the far field in aerodynamic simulations. Using lower resolution in such regions

*Associate Research Scientist; email: kmani@uwyo.edu.
†Professor; email: mavripl@uwyo.edu.

immediately frees up essential resources to focus on high gradient regions such as shock waves, boundary layers, contact discontinuities and wakes that exist closer to the aerodynamic body of interest. The same argument applies to the time domain and computational savings can be achieved by focusing temporal resolution on regions of the time domain where such resolution is necessary. While the locations of high gradient spatial features are to a certain extent known a priori, the locations of similar interesting features in the time domain are generally not known ahead of time and the use of an error indicator becomes necessary.

Several methods currently exist for time-step size control based on temporal discretization error. The purpose of such methods is to adaptively change the time-step size in various regions of the time domain resulting in overall reduction in computational expense with minimal loss in solution accuracy. Local error-based methods[4,13,14] use temporal discretizations of different orders of accuracy for the time derivative term in the governing equations in order estimate the local temporal discretization error. Higher temporal resolution (i.e. smaller and more time-steps) is used in regions of the time domain where the local temporal discretization error is high and lower resolution is used in regions of low local error. Goal-based or global error-based methods[15,16] determine the distribution of the temporal discretization error that is relevant to functional quantities of interest and similarly adapt the time-step size to improve functional accuracy.

While non-uniform spacing in the time domain is essential to reducing overall simulation cost, a fundamental point that is overlooked here is that resolution in the spatial and temporal domains can be treated independently of each other. Just as spatial flow gradients are small in the far field, it should be noted that there may large regions of the spatial domain where the temporal gradients also remain small. Much like the spatial flow gradients near the aerodynamic object of interest, it is quite likely that high temporal flow gradients exist only near features that exhibit strong unsteadiness such as moving shock waves or shedding vortices. The interpretation is that spatial elements with small temporal gradients do not have to be advanced in time at the same pace as spatial elements with high temporal gradients. This changes the traditional view on how unsteady problems are solved and opens a new avenue to explore for the reduction of computational cost. Since existing temporal error indicators (both local- and goal-based) construct the temporal error at each time-step as a straight sum or linear combination of the discrete distribution of this error over all spatial elements at the given time-step, the means already exist to identify individual spatial elements which require refinement in the time dimension.

The main hurdle is the development of efficient discretizations for the governing equations that permit non-uniform advancement in time. This paper presents a method to overcome this problem by treating the governing equations in integral form over space-time elements which have a constant cell averaged state over the entire element in space and time. While there have been a few attempts to solve the governing equations in space-time integral form,[17–19] advancing spatial elements non-uniformly in time has mostly been limited to explicit time-integration schemes.

It should be noted that in the work presented in this paper no attempt is made to adapt the spatial domain. Hence there is direct correspondence between spatial elements at different times and there are no spatial discontinuities going from one point in time to another within the same space-time element. However, there exists discontinuities in time going from one point in space to another.

Both local error-based and adjoint-based error indicators are investigated for use with the proposed method to idenfify regions in space-time that require higher temporal resolution.

II. Analysis Problem Formulation

A. Governing equations of the flow Problem in ALE form

We begin with the traditional conservative form of the Euler equations. In vectorial form the conservative form of the Euler equations may be written as:

$$\frac{\partial \mathbf{U}(\mathbf{x},t)}{\partial t} + \nabla \cdot \mathbf{F}(\mathbf{U}) = 0 \tag{1}$$

where the state vector $\mathbf{U}$ of conserved variables and the cartesian inviscid flux vector $\mathbf{F} = (\mathbf{F}^x, \mathbf{F}^y)$ are:

$$\mathbf{U} = \begin{pmatrix} \rho \\ \rho u \\ \rho v \\ E_t \end{pmatrix}, \quad \mathbf{F}^x = \begin{pmatrix} \rho u \\ \rho u^2 + p \\ \rho uv \\ u(E_t + p) \end{pmatrix}, \quad \mathbf{F}^y = \begin{pmatrix} \rho v \\ \rho uv \\ \rho v^2 + p \\ v(E_t + p) \end{pmatrix}, \tag{2}$$

Here ρ is the fluid density, (u,v) are the cartesian fluid velocity components, p is the pressure and E_t is the total energy. For an ideal gas, the equation of state relates the pressure to total energy by:

$$p = (\gamma - 1)\left[E_t - \frac{1}{2}\rho(u^2+v^2)\right] \tag{3}$$

where $\gamma = 1.4$ is the ratio of specific heats. Applying the divergence theorem and integrating over a moving control volume $A(t)$ that is bounded by the control surface $B(t)$ yields:

$$\int_{A(t)} \frac{\partial \mathbf{U}}{\partial t} dA + \int_{B(t)} \mathbf{F}(\mathbf{U}) \cdot \mathbf{n} dB = 0 \tag{4}$$

Using the differential identity:

$$\frac{\partial}{\partial t}\int_{A(t)} \mathbf{U} dA = \int_{A(t)} \frac{\partial \mathbf{U}}{\partial t} dA + \int_{B(t)} (\dot{\mathbf{x}} \cdot \mathbf{n}) dB \tag{5}$$

equation (4) is rewritten as:

$$\frac{\partial}{\partial t}\int_{A(t)} \mathbf{U} dA + \int_{B(t)} [\mathbf{F}(\mathbf{U}) - \dot{\mathbf{x}}\mathbf{U}] \cdot \mathbf{n} dB = 0 \tag{6}$$

or when considering cell-averaged constant values within each spatial element for the state $\mathbf{U}$, as:

$$\frac{dA\mathbf{U}}{dt} + \int_{B(t)} [\mathbf{F}(\mathbf{U}) - \dot{\mathbf{x}}\mathbf{U}] \cdot \mathbf{n} dB = 0 \tag{7}$$

This is the Arbitrary-Lagrangian-Eulerian (ALE) finite-volume form of the Euler equations. The equations are required in ALE form since the problem involves deforming meshes where mesh elements change in shape and size in time. Here A refers to the area or volume of the spatial element, $\dot{\mathbf{x}}$ is the vector of spatial mesh face or edge velocities, $\mathbf{n}$ is the unit normal of the face or edge, and B refers to the area or length of the bounding surface or edge.

Since the goal is to adapt the time-step size locally for each spatial element in the mesh, the ALE finite-volume form shown in equation (7) is further integrated in time to obtain the finite-volume formulation in space-time as:

$$\int_T \left\{ \frac{dA\mathbf{U}}{dt} + \int_{B(t)} [\mathbf{F}(\mathbf{U}) - \dot{\mathbf{x}}\mathbf{U}] \cdot \mathbf{n} dB \right\} dt = 0 \tag{8}$$

where separating the time integral yields:

$$\int_T \frac{dA\mathbf{U}}{dt} dt + \int_T \int_{B(t)} [\mathbf{F}(\mathbf{U}) - \dot{\mathbf{x}}\mathbf{U}] \cdot \mathbf{n} dB dt = 0 \tag{9}$$

B. The space-time element

Figure (1) illustrates a space-time element constructed using an arbitrary spatial element ABC at two different time indices n and $n-1$. This can also be interpreted as a space-time element bounded by two temporal faces which are defined by the spatial elements ABC at the two time indices. The spatial components of the normal vector for the temporal faces are zero by definition of the problem. The space-time element is also bounded on the sides by space-time faces. These faces are inclined due to spatial mesh deformation in time and usually have nonzero spatial and temporal normal vector components. Temporal faces are bounded by spatial edges and space-time faces are bounded by both temporal and spatial edges. Temporal edges connect the tails or heads of spatial edges at different times as shown in the figure. Figure (2) illustrates an example of a space-time face. There may be multiple temporal edges between two spatial edges in time because of neighboring space-time elements which take multiple time-steps in relation to the space-time element under consideration. Every edge (temporal or spatial) connects to a space-time node. It should also be noted that the top and bottom defining spatial edges of a space-time face are always oriented in the same direction. Temporal edges are always oriented such that they point in the direction of advancing time.

C. Temporal discretization

The solution state $\mathbf{U}$ is assumed to be constant within each space-time element and hence at any interface between space-time elements in the time dimension, the solution is double valued. Based on these assumptions, the time derivative term may be discretely represented as:

$$\int_T \frac{dA\mathbf{U}}{dt} dt = \frac{dA\mathbf{U}}{dt} \Delta t \tag{10}$$

where Δt refers to the height of the space-time element in the time dimension. The time derivative term is discretized using a first-order accurate BDF1 (Backward Difference Formula 1) scheme as:

$$\frac{dA\mathbf{U}}{dt} \Delta t = A^n \mathbf{U}^n - A^{n-1} \mathbf{U}^{n-1} \tag{11}$$

where $\mathbf{U}^n$ refers to the solution state within the space-time element extending from t^{n-1} and t^n, $\mathbf{U}^{n-1}$ refers to the solution state in the lower space-time element, and A^{n-1}, A^n refer to the temporal face areas. This discretization essentially amounts to a fully upwinded flux balance in the time dimension for the space-time element under consideration, accurate up to first-order, where the unit time normal for the upper face is 1 and the unit time normal for the lower face is -1. All spatial components of the normal vector for the upper and lower temporal faces are zero by definition of the problem.

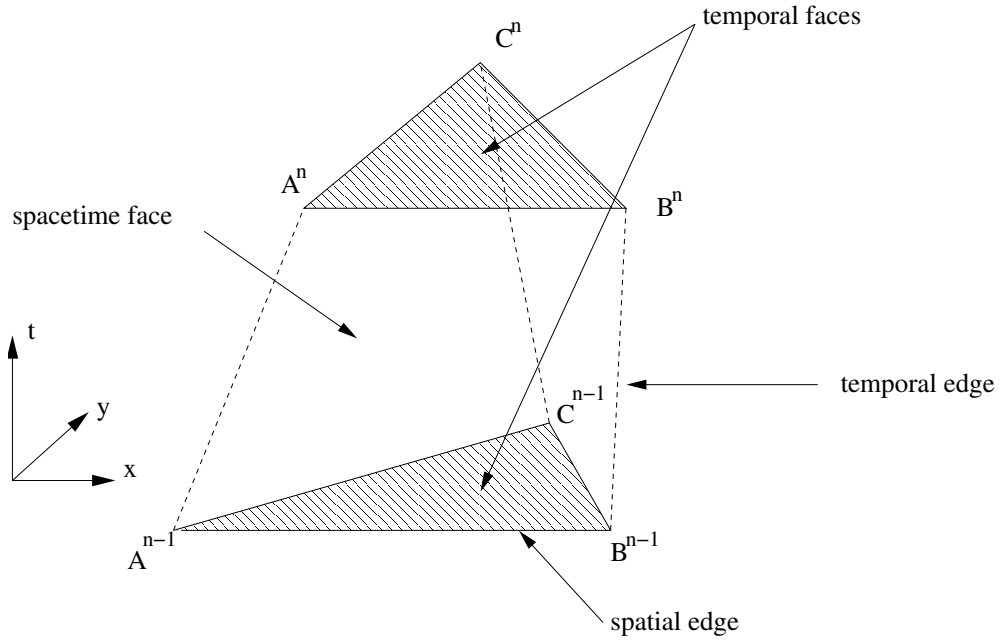

Figure 1. Example of a space-time element constructed from a spatial element at two time locations.

D. Spatial discretization

The flow solver uses a cell-centered finite-volume formulation where the inviscid flux integral S over the inclined space-time faces (i.e. with non-zero spatial components for the normal vector) bounding a space-time element is discretized as:

$$S = \int_T \int_{dB(t)} [\mathbf{F}(\mathbf{U}) - \dot{\mathbf{x}}\mathbf{U}] \cdot \mathbf{n} dB dt = \sum_{i=1}^{n_{edge}} \mathbf{F}_{e_i}^{\perp}(V_{e_i}, \mathbf{U}, \mathbf{n}_{ei}) B_{e_i} \Delta t_{e_i} \tag{12}$$

where B_e represents the L_2 norm of the spatial components of the dimensional normal vector of the face, V_e is the normal face velocity, $\mathbf{n}_e$ is the unit spatial normal vector of the face and is obtained by normalizing the dimensional spatial normal components of the face by B_e, $F_e^{\perp}$ is the normal convective flux across the face, and Δt_e is the height

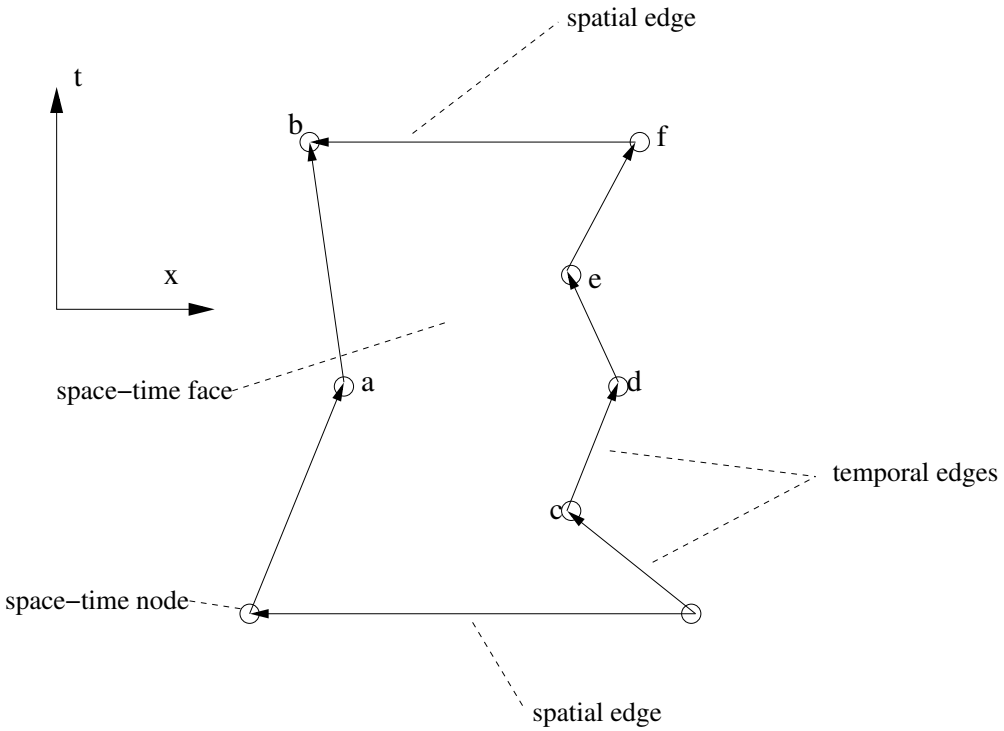

Figure 2. Example of a space-time face bounding a space-time element.

of the face in the time dimension. The normal convective flux across the face is computed using the second-order accurate matrix dissipation scheme[20] as the sum of a central difference and an artificial dissipation term as shown below,

$$\mathbf{F}_e^{\perp} = \frac{1}{2}\left\{\mathbf{F}_L^{\perp}(\mathbf{U}_L, V_e, \mathbf{n}_e) + \mathbf{F}_R^{\perp}(\mathbf{U}_R, V_e, \mathbf{n}_e) + \kappa^{(4)}[T]|[\lambda]|[T]^{-1}\left\{(\nabla^2\mathbf{U})_L - (\nabla^2\mathbf{U})_R\right\}\right\} \tag{13}$$

where $\mathbf{U}_L$, $\mathbf{U}_R$ are the left and right state vectors and $(\nabla^2\mathbf{U})_L$, $(\nabla^2\mathbf{U})_R$ are the left and right undivided Laplacians computed for any space-time element i as

$$(\nabla^2\mathbf{U})_i = \sum_{k=1}^{\text{spatial neighbors}} (\mathbf{U}_k - \mathbf{U}_i) \tag{14}$$

The matrix $[\lambda]$ is diagonal and consists of the eigenvalues (adjusted by normal edge velocity V_e) of the flux Jacobian matrix $\frac{\partial \mathbf{F}^{\perp}}{\partial \mathbf{U}}$, and the matrix $[T]$ consists of the corresponding eigenvectors. The scalar parameter $\kappa^{(4)}$ is empirically determined and controls the amount of artificial dissipation added to the centrally differenced flux. For transonic problems this is usually taken as 0.1. The advantage of using the difference of the undivided Laplacians in the construction of the convective flux is that it offers second-order spatial accuracy without the need for state reconstruction techniques. The normal native flux vector is computed as

$$\mathbf{F}^{\perp} = \begin{pmatrix} \rho(V^{\perp} - V_e) \\ \rho(V^{\perp} - V_e)u + \hat{n}_x p \\ \rho(V^{\perp} - V_e)v + \hat{n}_y p \\ E_t(V^{\perp} - V_e) + pV^{\perp} \end{pmatrix} \tag{15}$$

where the fluid velocity normal to the edge $V^{\perp}$ is defined as $u\hat{n}_x + v\hat{n}_y$, where $\hat{n}_x$ and $\hat{n}_y$ are the spatial components of the unit face normal vector.

E. Mesh deformation strategy

Deformation of the mesh is achieved through the linear tension spring analogy[21,22] which approximates the complete space-time mesh as a network of inter-connected springs. Every spatial and temporal edge defines a spring connected to a space-time node. The spring coefficient is assumed to be inversely proportional to the edge length. Three independent force balance equations for x, y and t are formulated for each node based on displacements of neighboring nodes. This results in a nearest neighbor stencil for the final linear system to be solved. The linear system that relates the interior node displacements in the mesh to known displacements on the boundaries is given as

$$\mathbf{G}(\mathbf{x}) = [\mathbf{K}]\delta\mathbf{x}_{int} - \delta\mathbf{x}_{bound} = 0 \tag{16}$$

where $[\mathbf{K}]$ is the stiffness matrix assembled using the spring coefficients of each of the edges in the computational mesh. Since the equations are decoupled between dimensions, prescribing zero displacements in the time dimension at the boundaries assures that temporal faces have zero spatial normal vector components. The linear mesh motion system is solved using restarted GMRES[23] iterations with 20 Krylov vectors.

F. The discrete geometric conservation law (GCL) and space-time face normals

The discrete geometric conservation law (GCL) requires that a uniform flow field be preserved exactly when equation (9) is integrated. In other words the deformation of the computational mesh should not introduce conservation errors in the solution of the flow problem. This translates into $\mathbf{U} = constant$ being an exact solution of equation (9). The space-time face velocities and normal vectors have to be chosen such that this condition is satisfied.

The normal space-time face velocity including the spatiotemporal area of the face can be computed as follows. Collapsing the two spatial edges defining the top and bottom of a space-time face to the same time level, the face can be viewed as an area swept in x, y by a spatial edge deforming from its orientation at time index $n-1$ to its new orientation at time index n. The path followed by the head and tail nodes of the spatial edge between the two orientations is given by the spatial coordinates of the head nodes belonging to the intermediate temporal edges. The area swept by the spatial edge is computed using the Green-Gauss contour integral and used as the face velocity which includes the space-time face area.

Only the dimensional spatial components of the space-time face normal vector are required and these are computed using the time-averaged coordinates of the head and tail nodes belonging to the sweeping spatial edge between the two orientations. Choosing the space-time face normal velocities and face normal vectors in this manner assures that for a constant flow field, the governing equations discretely integrate in space-time to zero.

III. Space-Time Implicit Solution Procedure

Consider the normal case of uniformly advancing spatial elements in time. For the first-order BDF1 time-integration scheme, the flow equations are solved implicitly at each time-step by introducing an implicit residual $\mathbf{R}$ as:

$$\mathbf{R}^n(\mathbf{U}^n, \mathbf{U}^{n-1}, \mathbf{x}^n, \mathbf{x}^{n-1}) = 0 \tag{17}$$

which is linearized with respect to the unknown state $\mathbf{U}^n$ and solved using Newton's method as:

$$\begin{aligned} \left[\frac{\partial \mathbf{R}(\mathbf{U}^k, \mathbf{x})}{\partial \mathbf{U}^k}\right] \delta\mathbf{U}^k &= -\mathbf{R}(\mathbf{U}^k, \mathbf{x}) \\ \mathbf{U}^{k+1} &= \mathbf{U}^k + \delta\mathbf{U}^k \\ \delta\mathbf{U}^k \to 0, \mathbf{U}^{k+1} &= \mathbf{U}^n \end{aligned} \tag{18}$$

In the case of a uniform time-step size for all spatial elements, the state vector $\mathbf{U}$ for each spatial element is unknown at time-index n but is known at the previous time index $n-1$. The solution procedure involves constructing the nonlinear residual $\mathbf{R}$ for each spatial element at the time index n and solving for the state $\mathbf{U}^n$ using Newton's method, where the intermediate linear systems arising in the non-linear solution are solved approximately by any choice of linear solver. In this work the preconditioned GMRES algorithm with ILU(0) as the preconditioner is used.

Figures (3(a)) and (3(b)) illustrate the uniform advancement in time with and without the presence of spatial mesh deformation in time for a spatially one-dimensional problem.

In the case of spatially nonuniform time stepping, neighboring spatial elements are advanced in time at different rates. The solution procedure for such a problem involves first dividing the time domain into slabs of some predetermined temporal spacing and then subdividing certain space-time elements appropriately in the time dimension when

additional temporal resolution is required. The temporal slab thickness is chosen such that essential nonlinearities in the time dimension are captured. The advancement in time is now carried out from slab to slab, where the solution state $\mathbf{U}$ for all space-time elements in a particular slab are solved for simultaneously in an implicit manner before moving onto the next slab in time. The residual operator for a slab can be written as:

$$\mathbf{R}^n(\mathbf{U}^n, \mathbf{U}^b, \mathbf{x}^n, \mathbf{x}^b) = 0 \tag{19}$$

where the index n now refers to a temporal slab and all of the space-time elements contained within it. The index b refers to boundary values for the slab in both space and in time. The solution process involves applying Newton's method on the nonlinear residual operator $\mathbf{R}$ defined over the entire temporal slab. It is important to note that the state vectors of each space-time element in the slab under consideration are unknown and have to be obtained simultaneously irrespective of their location in time within the slab. Figures (4(a)) and (4(b)) illustrate the time advancement procedure for spatially nonuniform time stepping with and without the presence of mesh deformation.

A comparison of the typical non-linear convergence of the flow equations at a single time-step for the case of uniform time-stepping and a single slab for the case of non-uniform time-stepping is shown in Figure (5(a)). The number of non-linear iterations required for solution convergence is approximately the same between the spatially non-uniform and spatially uniform time-stepping cases. In addition it can be seen from Figure (5(b)) that the number of non-linear iterations remain roughly the same even as the number of unknowns in the time slab is increased. The strong implicitness of ILU(0) as a preconditioner for GMRES results in a nearly mesh resolution independent solver.

Quadratic convergence of the non-linear problem is achievable provided the flow Jacobian matrix is exact and the linear system is solved to machine precision. However, constructing and storing the exact flow Jacobian matrix for a spatially second-order accurate solver especially on non-conforming unstructured meshes such as those proposed in this work is impractical due to the lack of simple data structures. A key advantage of the preconditioned GMRES algorithm is that it only requires the residual of the linear system shown in equation (18) and a suitable preconditioner. Explicit storage of only the preconditioner is necessary and not the actual flow Jacobian matrix itself. This aspect of the algorithm can be exploited because construction of the product of the exact flow Jacobian with a vector is done efficiently following the pattern in the code used to compute the residual. Incomplete LU-factorization with zero fill-in of the first-order accurate approximate flow Jacobian is stored and passed to the GMRES algorithm for use as the preconditioner. Near quadratic convergence is observed in both Figures (5(a)) and (5(b)). For the work presented here, the GMRES algorithm uses 20 Krylov vectors with 20 restarts. While these parameter values create an efficient linear solver, they are not sufficient to solve the linear system to machine precision and hence the deviation from textbook quadratic convergence.

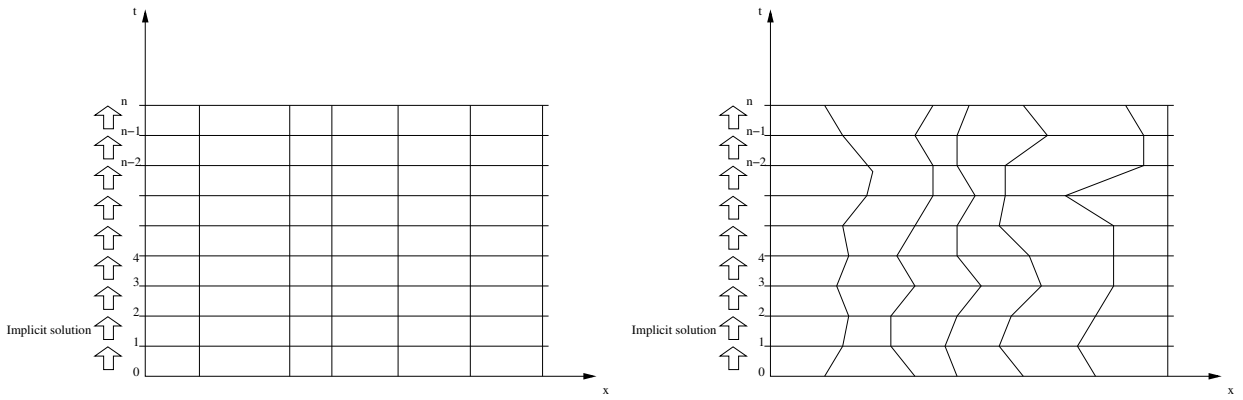

(a) Spatially uniform time stepping without mesh deformation

(b) Spatially uniform time stepping with spatial mesh deformation

Figure 3. Illustration of spatially uniform time stepping for a spatially one-dimensional problem.

IV. Adjoint-Based Functional Error Formulation

Consider a functional computed based on the unsteady solutions of the flow and mesh motion equations. Mathematically this may be represented as $L = L(\mathbf{U}, \mathbf{x})$ where L is the functional, $\mathbf{U}$ is the unsteady flow solution set and $\mathbf{x}$ is the set of unsteady mesh solutions. The functional evaluated on two different space-time meshes of discrete resolutions h and H can represented by $L_h(\mathbf{U}_h, \mathbf{x}_h)$ and $L_H(\mathbf{U}_H, \mathbf{x}_H)$. For the purpose of this paper, H refers to some arbitrary

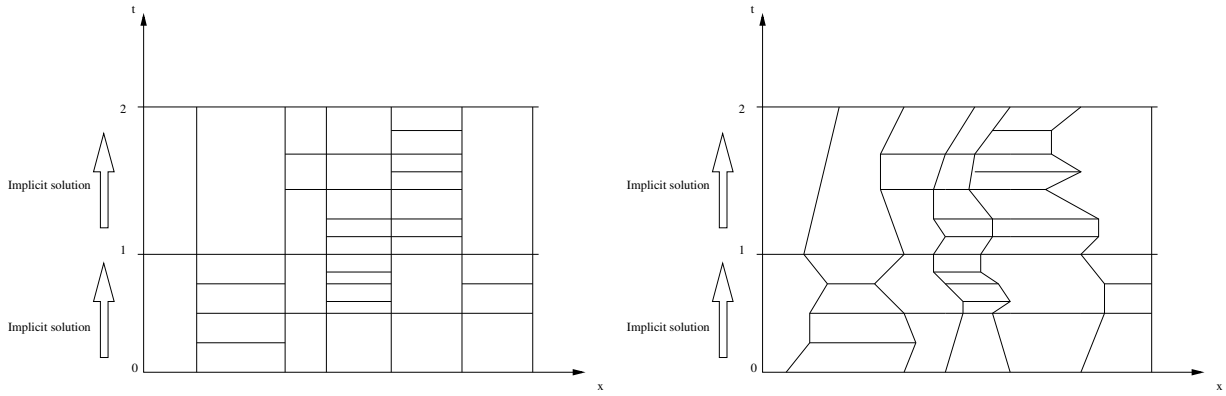

(a) Spatially nonuniform time stepping without mesh deformation (b) Spatially nonuniform time stepping with spatial mesh deformation

Figure 4. Illustration of spatially nonuniform time stepping for a spatially one-dimensional problem.

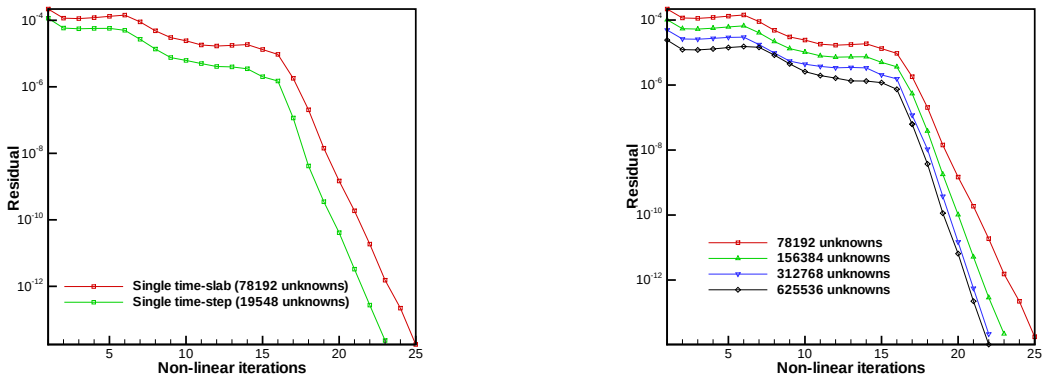

(a) Single time-step vs time-slab (b) Time-slabs with different resolutions.

Figure 5. Comparison of non-linear convergence of different systems

coarse resolution space-time mesh and h is a fine resolution space-time mesh constructed by nested subdivision in the time dimension of each space-time element in H using a ratio of 2-to-1. An estimate of $L_h(\mathbf{U}_h, \mathbf{x}_h)$ can be obtained based on the Taylor expansion around the functional $L_h(\mathbf{U}_h^H, \mathbf{x}_h^H)$, where $\mathbf{U}_h^H$ and $\mathbf{x}_h^H$ refer to projections of the flow and mesh solutions from the coarse to the fine level. Assuming that the coarse space-time domain flow solution $\mathbf{U}_H$ and the coarse space-time domain mesh coordinates $\mathbf{x}_H$ have been obtained via full convergence of the respective equations, the Taylor series expansion of the exact fine space-time domain functional can be written as:

$$L_h(\mathbf{U}_h, \mathbf{x}_h) = L_h(\mathbf{U}_h^H, \mathbf{x}_h^H) + \left[\frac{\partial L}{\partial \mathbf{U}}\right]_{\mathbf{U}_h^H, \mathbf{x}_h^H} \left(\mathbf{U}_h - \mathbf{U}_h^H\right) + \left[\frac{\partial L}{\partial \mathbf{x}}\right]_{\mathbf{x}_h^H, \mathbf{U}_h^H} \left(\mathbf{x}_h - \mathbf{x}_h^H\right) + \cdots \tag{20}$$

The procedure for computing an unsteady solution involves obtaining the solution to the non-linear residual operator $\mathbf{R}(\mathbf{U}, \mathbf{x})$ within each temporal slab. The non-linear operator $\mathbf{R}(\mathbf{U}, \mathbf{x})$ is constructed by the previously described discretization of the governing flow equations. Expanding a fine space-time domain residual set about the coarse space-time domain set of residuals yields:

$$\mathbf{R}_h(\mathbf{U}_h, \mathbf{x}_h) = \mathbf{R}_h(\mathbf{U}_h^H, \mathbf{x}_h^H) + \left[\frac{\partial \mathbf{R}}{\partial \mathbf{U}}\right]_{\mathbf{U}_h^H, \mathbf{x}_h^H} \left(\mathbf{U}_h - \mathbf{U}_h^H\right) + \left[\frac{\partial \mathbf{R}}{\partial \mathbf{x}}\right]_{\mathbf{x}_h^H, \mathbf{U}_h^H} \left(\mathbf{x}_h - \mathbf{x}_h^H\right) + \cdots = 0 \tag{21}$$

and since the non-linear residual operator $\mathbf{R}$ must vanish for a converged solution within each time slab, an estimate for the error vector $(\mathbf{U}_h - \mathbf{U}_h^H)$ in equation (20) can obtained by rearranging equation (21) as:

$$\left(\mathbf{U}_h - \mathbf{U}_h^H\right) \approx -\left[\frac{\partial \mathbf{R}}{\partial \mathbf{U}}\right]^{-1}_{\mathbf{U}_h^H, \mathbf{x}_h^H} \left\{ \mathbf{R}_h(\mathbf{U}_h^H, \mathbf{x}_h^H) + \left[\frac{\partial \mathbf{R}}{\partial \mathbf{x}}\right]_{\mathbf{x}_h^H, \mathbf{U}_h^H} \left(\mathbf{x}_h - \mathbf{x}_h^H\right) \right\} \tag{22}$$

It should be noted that this is merely an estimate for the error between $\mathbf{U}_h$ and $\mathbf{U}_h^H$ since higher-order terms in the Taylor expansion are ignored. Substituting equation (22) into equation (20) results in:

$$L_h(\mathbf{U}_h, \mathbf{x}_h) \approx L_h(\mathbf{U}_h^H, \mathbf{x}_h^H) \underbrace{- \left[\frac{\partial L}{\partial \mathbf{U}}\right]_{\mathbf{U}_h^H, \mathbf{x}_h^H} \left[\frac{\partial \mathbf{R}}{\partial \mathbf{U}}\right]^{-1}_{\mathbf{U}_h^H, \mathbf{x}_h^H} \left\{ \mathbf{R}_h(\mathbf{U}_h^H, \mathbf{x}_h^H) + \left[\frac{\partial \mathbf{R}}{\partial \mathbf{x}}\right]_{\mathbf{x}_h^H, \mathbf{U}_h^H} \left(\mathbf{x}_h - \mathbf{x}_h^H\right) \right\} + \left[\frac{\partial L}{\partial \mathbf{x}}\right]_{\mathbf{x}_h^H, \mathbf{U}_h^H} \left(\mathbf{x}_h - \mathbf{x}_h^H\right)}_{\varepsilon_{cc}} \tag{23}$$

The right-hand-side in equation (23) can be described as an estimate for the exact functional evaluated directly on the fine space-time mesh. Based on the derivation it is approximately equal to the sum of the functional evaluated on the fine space-time mesh using a projected solution and projected mesh coordinates from the coarse space-time mesh and a computable correction term ε_{cc}.

The correction term ε_{cc} as defined above is:

$$\varepsilon_{cc} = -\left[\frac{\partial L}{\partial \mathbf{U}}\right]_{\mathbf{U}_h^H, \mathbf{x}_h^H} \left[\frac{\partial \mathbf{R}}{\partial \mathbf{U}}\right]^{-1}_{\mathbf{U}_h^H, \mathbf{x}_h^H} \left\{ \mathbf{R}_h(\mathbf{U}_h^H, \mathbf{x}_h^H) + \left[\frac{\partial \mathbf{R}}{\partial \mathbf{x}}\right]_{\mathbf{x}_h^H, \mathbf{U}_h^H} \left(\mathbf{x}_h - \mathbf{x}_h^H\right) \right\} + \left[\frac{\partial L}{\partial \mathbf{x}}\right]_{\mathbf{x}_h^H, \mathbf{U}_h^H} \left(\mathbf{x}_h - \mathbf{x}_h^H\right) \tag{24}$$

Since computing, storing and inverting the flow Jacobian matrix is expensive, a flow adjoint variable $\Lambda_{\mathbf{U}}$ is defined to aid the evaluation procedure. The flow adjoint variable is defined as:

$$\Lambda_{\mathbf{U}_h^H}^T \big|_{\mathbf{U}_h^H \mathbf{x}_h^H} = -\left[\frac{\partial L}{\partial \mathbf{U}}\right]_{\mathbf{U}_h^H, \mathbf{x}_h^H} \left[\frac{\partial \mathbf{R}}{\partial \mathbf{U}}\right]^{-1}_{\mathbf{U}_h^H \mathbf{x}_h^H} \tag{25}$$

Transposing and rearranging equation (25) yields

$$\left[\frac{\partial \mathbf{R}_h}{\partial \mathbf{U}_h}\right]^T_{\mathbf{U}_h^H \mathbf{x}_h^H} \Lambda_{\mathbf{U}h} \big|_{\mathbf{U}_h^H, \mathbf{x}_h^H} = -\left[\frac{\partial L}{\partial \mathbf{U}}\right]^T_{\mathbf{U}_h^H, \mathbf{x}_h^H} \tag{26}$$

The solution of equation (26) involves projecting the coarse space-time flow solution and mesh coordinates onto the fine space-time mesh, reconstructing the flow Jacobian matrices on the fine space-time mesh and then solving the linear system iteratively for the flow adjoint variable. Since the goal is to avoid direct solutions of any nature on the fine space-time mesh, an approximation is used where the adjoint is evaluated on the coarse space-time mesh and then

projected onto the fine mesh. This circumvents the expensive evaluations on the fine mesh. Equation (26) recast on the coarse space-time mesh becomes:

$$\left[\frac{\partial \mathbf{R}}{\partial \mathbf{U}}\right]^T_{\mathbf{U}_H,\mathbf{x}_H} \Lambda_{\mathbf{U}H} = -\left[\frac{\partial L}{\partial \mathbf{U}}\right]^T_{\mathbf{U}_H,\mathbf{x}_H} \tag{27}$$

The coarse adjoint variable can then be projected onto to the fine domain as:

$$\Lambda_{\mathbf{U}h} = I_h^H \Lambda_{\mathbf{U}H} \tag{28}$$

where I_h^H is some appropriate projection operator. Once the vector of adjoint variables $\Lambda_{\mathbf{U}H}$ has been obtained the first contributions to the computable correction term may be determined by projecting the flow adjoint onto the fine space-time mesh and then evaluating a vector inner product as follows:

$$\varepsilon_{cc_1} = {\Lambda_{\mathbf{U}_h^H}}^T R_h(\mathbf{U}_h^H, \mathbf{x}_h^H) \tag{29}$$

ε_{cc_1} represents the contribution from the flow equations to the error arising due to insufficient temporal resolution within each space-time element. The residual $\mathbf{R}_h(\mathbf{U}_h^H, \mathbf{x}_h^H)$ is non-zero since it is computed using the projection of the coarse space-time flow solution onto the fine space-time mesh. Closer examination reveals that equation (29) is actually a summation of the inner products of the flow adjoint and the non-zero residual within each space-time element on the fine space-time mesh. The remaining contributions to the total correction term may be written in combined form as:

$$\varepsilon_{cc_2} = \left\{ \Lambda_{\mathbf{U}_h}^T \left[\frac{\partial \mathbf{R}_h}{\partial \mathbf{x}_h}\right]_{\mathbf{U}_h^H \mathbf{x}_h^H} + \left[\frac{\partial L_h}{\partial \mathbf{x}_h}\right]_{\mathbf{x}_h^H} \right\} \left(\mathbf{x}_h - \mathbf{x}_h^H\right) = \lambda_{\mathbf{x}} \left(\mathbf{x}_h - \mathbf{x}_h^H\right) \tag{30}$$

using the notation $\lambda_{\mathbf{x}}$ as shorthand for the large bracketed term in the middle of the above equation. We now write a Taylor expansion of the mesh residual equation $\mathbf{G}$ on the fine space-time mesh about its value constructed using projected mesh coordinates from the coarse to the fine meshes as:

$$\mathbf{G}(\mathbf{x}_h) \quad = \quad \mathbf{G}(\mathbf{x}_h^H) + \left[\frac{\partial \mathbf{G}}{\partial \mathbf{x}}\right]_{\mathbf{x}_h^H} (\mathbf{x}_h - \mathbf{x}_h^H) + \cdots = 0 \tag{31}$$

Here the residual $\mathbf{G}(\mathbf{x}_h^H)$ is evaluated using the projected values for $\mathbf{x}_{int}$ from the coarse space-time mesh to the fine mesh and the exact values of $\mathbf{x}_{bound}$ on the fine space-time mesh. The boundary coordinates $\mathbf{x}_{bound}$ are only a function of time and can be easily evaluated on the fine space-time mesh. Rearranging and simplifying the mesh residual Taylor expansion yields:

$$(\mathbf{x}_h - \mathbf{x}_h^H) = -\left[\frac{\partial \mathbf{G}}{\partial \mathbf{x}}\right]^{-1}_{\mathbf{x}_h^H} \mathbf{G}(\mathbf{x}_h^H) \tag{32}$$

However, refering to Equation (16) it is seen that the linearization of the mesh residual $\mathbf{G}$ with respect to the mesh coordinates $\mathbf{x}$ is simply the mesh stiffness matrix $[\mathbf{K}]$. Therefore,

$$(\mathbf{x}_h - \mathbf{x}_h^H) = -[\mathbf{K}]^{-1} \mathbf{G}(\mathbf{x}_h^H) \tag{33}$$

Substituting this back into equation (30) gives us an expression for the second and final contribution to the computable correction term as:

$$\varepsilon_{cc_2} = -\lambda_{\mathbf{x}_h} [\mathbf{K}]^{-1} \mathbf{G}(\mathbf{x}_h^H) \tag{34}$$

Defining a mesh adjoint variable $\Lambda_{\mathbf{x}}$ permits an iterative solution and avoids inversion of the stiffness matrix.

$$[\mathbf{K}]^T \Lambda_{\mathbf{x}h} = -{\lambda_{\mathbf{x}_h}}^T \tag{35}$$

As in the case of the flow adjoint, the above system is solved on the coarse space-time mesh and the coarse mesh adjoint variable then projected onto the fine space-time mesh by some appropriate operator as:

$$[\mathbf{K}]^T \Lambda_{\mathbf{x}H} = -{\lambda_{\mathbf{x}H}}^T \tag{36}$$

$$\Lambda_{\mathbf{x}h} = I_h^H \Lambda_{\mathbf{x}H} \tag{37}$$

Both a mesh adjoint variable vector and a flow adjoint variable vector must be solved for within each time slab during the backward sweep in time. Details on the exact solution process involving the backward sweep in time can be found in Ref.[24] The final form for the second contribution to the correction term can now be expressed as:

$$\varepsilon_{cc_2} = \Lambda_{\mathbf{x}_h^H}^T \mathbf{G}(\mathbf{x}_h^H) \tag{38}$$

ε_{cc_2} represents the contribution from the mesh motion equations to the temporal resolution error. Just as in the case of the temporal resolution error due to the flow equations, equation (38) represents a summation of inner products of the mesh adjoint and the mesh residual within each space-time element. Although the mesh motion equations are linear, the resulting mesh coordinate variations in time are not linear, since these are driven by the prescribed surface mesh displacements, which in our following example are non-linear in time. This causes the mesh residual to be non-zero when computed on the fine space-time domain using projected mesh coordinates from the coarse space-time domain.

The contribution to the total correction from each space-time element can be interpreted as the representation of the error in the functional arising from that space-time element. The resulting distribution in space-time of the total error ε_{cc} can thus be conveniently used as the criteria for identifying regions in space-time that require higher temporal resolution.

V. General Implementation Details

The space-time adaptive solver consists of four separate codes, namely a mesh preprocessor, a mesh adaptation code, the flow solver and the adjoint solver. The mesh preprocessor takes in a standard unstructured spatial mesh and constructs a space-time mesh based on the chosen temporal parameters for the flow problem. The required temporal parameters are the number of temporal slabs for the unsteady problem and the thickness (in time) of each temporal slab. Slabs are normally taken to be of uniform thickness, although varying thicknesses are permitted. The initial mesh is constructed such that each spatial element in the slab consists of two uniform time-steps to begin with. This is done mainly to simplify coding of certain aspects of the mesh preprocessor.

The flow solver computes a solution using this space-time mesh and also writes out the solution to the hard drive in a piecewise manner (slab-by-slab) during the solution process. The adjoint solver is then invoked which reads in the solution from the hard drive and performs a backward sweep in time to compute the necessary adjoint variables. The adjoint solver also constructs the residuals on the fine space-time mesh and estimates the functional error by performing the inner product between the adjoint variables and the residuals. Space-time elements are first ranked by their contribution to the total predicted error in the functional, and then working downward from the element with the highest contribution, elements are flagged for refinement until 99% of the total error has been accounted for.

The mesh adaptation routine takes in the old space-time mesh and the list of space-time elements that have been flagged for refinement and constructs a new space-time mesh. Space-time elements that are to be refined are subdivided into two elements of equal lengths in the time dimension. A maximum time-step size ratio of two is strictly enforced between neighboring space-time elements in the space dimension in order avoid large jumps in the time-step sizes of neighbors. However, this ratio is currently not enforced in the temporal direction. Once the new space-time mesh has been constructed, it is written to disk and picked up by the flow solver for the next unsteady solution. This overall process represents a single adaptation cycle.

Since at any adaptation cycle, a space-time element is at most subdivided into two, comparisons are made against uniform time-stepping where the number of time-steps is increased by a factor of two and the time-step sizes are reduced by a factor of two for all spatial elements.

VI. Results

A. Case 1: Transonic pitching airfoil

The first example is that of a transonic pitching NACA64A010 airfoil. The airfoil pitches sinusoidally around its quarter-chord location in a free-stream Mach number of 0.8 with a mean angle-of-attack of zero. The amplitude of pitch is 2.5 degrees and the reduced frequency is 0.1. The time domain for this problem was chosen such that two pitch periods are completed starting from a zero angle-of-attack. The unsteady solution is initiated using the steady solution around the airfoil at zero angle-of-attack. The first quarter of the first pitch cycle is modified to follow a scaled and phase shifted cosine profile rather than the default sinusoidal profile in order to assure a smooth rather than an impulsive start of the unsteady motion from steady state.

The spatially non-uniform time-stepping case consists of 32 equally sized temporal slabs of temporal thickness

1.96349540849362 in non-dimensional time. The spatially uniform time-stepping case begins with 32 time steps, with time-step size equal to the thickness of a single slab. Figure (6) shows the spatial mesh for this problem and consists of 6601 spatial elements. No mesh deformation equations are solved for this particular case since prescribed mesh rotations are applied to every single mesh node. The adjoint-based error indicator is employed for adaptation of the space-time mesh for this example problem. The lift coefficient of the airfoil at the final time is used as the target functional. All comparisons are made against a reference functional computed using a solution obtained with 10000 uniform time steps. Adaptation was terminated after 6 cycles for the spatially non-uniform and temporally uniform time-stepping cases.

Figures (7(a)) and (7(b)) show the convergence of the functional and the error in the functional with respect to the total degrees-of-freedom in the problem. For the spatially non-uniform time-stepping case the total degrees-of-freedom is the total number of space-time elements from all slabs, while for the spatially uniform time-stepping case it is equal to the number of spatial elements multiplied with the number of time steps. The plot indicates that adjoint-based adaptation with spatially non-uniform time-stepping is able to outperform uniform time-stepping with uniform time-step sizes. For a functional error level of $1e^{-4}$ a reduction in the number of degrees-of-freedom by a factor of 5 is observed. When the functional correction term provided by the adjoint is included, a factor of approximately 8 is observed.

Figures (8(a)) through (8(f)) show the initial spatial distribution of the functional relevant temporal error within various time slabs before any adaptation has occurred. As expected, the adjoint-based error indicates that high temporal gradient features such as the moving shock waves on the upper and lower surfaces of the airfoil have to be stepped with high resolution in time. The figures also show the expected trend of progressively higher temporal error in time slabs closer to the end of the time domain where the functional is evaluated. However, an unexpected result is that large spatial elements in the farfield also contribute significantly to the temporal error in the functional. This clearly demonstrates the advantage of using adjoint-based error estimates for adaptation. More importantly, the results also demonstrate the advantage of using a space-time framework to further harness the strength of adjoint equations and adapt the time-step size in a spatially local sense.

Figures (9(a)) through (9(f)) show the number of time-steps taken by spatial elements in the vicinity of the airfoil in various time slabs after the final adaptation cycle.

It can be seen that most of the elements near the airfoil take no more than 10 to 12 time-steps and there are also large regions particularly in the earlier time slabs which require only 2 time-steps. At least near the airfoil, up until the final time slab only a small band of spatial elements which contain the upper and lower surface shock waves take the largest number of time steps of 30. Figures (10(a)) through (10(f)) show time steps taken by spatial elements in the farfield within various slabs. It can be seen that several of the spatial elements in the farfield take 30 time steps within each slab leading up to the final time slab at which point their importance to the functional drops and they take no more than 2 time steps. The spatial sizes of the elements in these regions are large, indicating that only a few spatial elements require small time-steps. This results in considerable reduction of total degrees-of-freedom. By the same argument, significant reduction in total degrees-of-freedom is also realized from regions close to the airfoil that are covered by several small spatial elements but take very few time-steps.

Adjoint based adaptation pursues equidistribution of the functional relevant error throughout the space-time domain. Once this is achieved the method loses its usefulness and performs no better than uniform refinement since all spatial and temporal locations contribute the same level of error to the functional. Figures (11(a)) through (11(f)) show this trend of the error being fairly uniform at all spatial locations within all time slabs after adaptation has been terminated.

B. Case 2: Convecting vortex interacting with a pitching airfoil

The second example simulates the interaction of vortex convecting with free-stream with a slowly pitching subsonic NACA64A010 airfoil. The spatial mesh used for this example is shown in Figure (12) and is made up of 8600 elements. The freestream Mach number is 0.4225 for this problem and the airfoil pitches around its quarter-chord with a reduced frequency of 0.03. The amplitude of pitch is set to be 2.5 degrees and the mean angle-of-attack is zero. The vortex is seeded initially at a location 3 chords in front and 2 chords below the leading edge of the airfoil. Density contours of the initial condition for this problem can be seen in Figure (13). The time domain for this problem is between zero and 28 in non-dimensional time. This covers a quarter pitch period of the airfoil based on the chosen reduced frequency while the vortex convects 14 chord lengths. The time domain for the spatially non-uniform time-stepping case is divided up as 25 slabs with 4 time steps within each slab of size 0.28. The spatially uniform time-stepping case begins with 100 time steps of size 0.28 and is uniformly refined at each adaptation cycle. The linear mesh deformation equations are solved in this example problem so as to keep the outer boundary fixed while the airfoil pitches. The

functional chosen for this example is the lift coefficient of the airfoil integrated in time over the whole time domain. Figure (14) shows variation of the lift coefficient of the airfoil in time for this problem. The functional is simply the area under the curve. Comparisons are made against a reference functional obtained by solving the problem with 10000 uniform time steps. As with the previous example the adjoint-based error indicator is used to identify space time elements for adaptation.

Figures (15(a)) and (15(b)) show the convergence of the functional and the error in the functional with respect to the total degrees-of-freedom. Adaptation was terminated after 6 cycles for this case. For similar error levels it can be seen that spatially non-uniform time-stepping shows a reduction in degrees-of-freedom by a factor of approximately 3. When considering the corrected functional for similar levels, the factor of saving is approximately 5. Figures (16(a)) through (16(d)) shows the initial distribution of the functional relevant temporal error within various time slabs before the start of adaptation. The plots show the expected trend of high error tracking the vortex until it passes the airfoil after which the effect of the vortex is not important to the lift acting on the airfoil. Once the vortex has passed the airfoil, the error is primarily focused around the airfoil itself. Figures (17(a)) through (17(d)) show the number of time-steps taken by each spatial within various time slabs. Following the trend of the computed adjoint-based error, the spatial elements containing the vortex step slowly with as many as 120 steps while most of the spatial elements only take 10 steps. Once the vortex has passed the airfoil it continues convecting through the domain, but the no adaptation of the time-step size in and around the vortex at this point is necessary to improve the functional value. Instead the time-step size adaptation targets the spatial elements around the airfoil because the airfoil continues to pitch up thus affecting its lift. Figures (16(a)) through (16(d)) shows the distribution of the functional relevant error within various slabs after adaptation has been terminated. It can be seen that adaptation has led to relative uniformity of the error.

VII. Conclusion

A space-time finite-volume formulation was developed to treat both space and time dimensions in a unified manner. The method permits non-uniform advancement of spatial elements in time and offers reduction of overall degrees-of-freedom in unsteady flow solutions. Both example cases presented show that significant reduction in the total number of unknowns is possible when adapting the time-step size in a spatially local sense. This was acheived through the use of the adjoint weighted residual method as the error indicator to identify space-time regions that require higher temporal resolution. The cost of solving the adjoint equations to determine the functional relevant error distribution is similar to the cost of solving the primal flow problem in the space-time framework. Therefore overall a single adaptation cycle costs approximately twice that of just the primal problem. It has also been shown that the number of non-linear iterations required to solve the primal problem within each slab is roughly remains roughly the same as the number of non-linear iterations required for the primal problem at each time-step when advancing all spatial elements uniformly in time. This in theory implies that the cost of solving the primal problem is a direct function of the number of degrees-of-freedom, and thus any reduction in unknowns should translate into a reduction in computational expense. Applying a factor of two to the overall factor of savings in number of unknowns to compensate for the cost of obtaining the adjoint should in theory still yield reduction in computational expense of a factor anywhere between 1.5 and 3 for the problems presented in this paper. However, it has been noticed that coding inefficiences have resulted in non-linear increases in the cost of solving the primal problem as the system size grows during the course of the adaptation procedure eventhough the number of non-linear iterations per implicit (slab) solution remains roughly the same. Addressing such issues should further strengthen the usefulness of this method.

Future work in addition to coding improvements would involve further developing the solver for application to viscous and turbulent flows in two dimensions. Extension to three dimensions of the methodology currently remains unfeasible due to the extraordinarily high memory requirements. Ultimately, the developed method for solving unsteady problems should find applications particularly in the context of rotorcraft and wind turbines, where large differences exist between the flow close to the hub and flow close to the tips of the blades.

References

[1]Jameson, A., Schmidt, W., and Turkel, E., "Numerical Solutions of the Euler Equations by Finite Volume Methods Using Runge-Kutta Time-Stepping Schemes," *AIAA 14th Fluid and Plasma Dynamic Conference, Palo Alto, CA*, 1981, AIAA Paper 81–1259.

[2]Jameson, A., "Time Dependent Calculations Using Multigrid, with Applications to Unsteady Flows Past Airfoils and Wings," *AIAA 10th Computational Fluid Dynamics Conference, Honolulu, HI*, 1991, AIAA Paper 91–1596.

[3]Carpenter, M. H., Viken, S., and Nielsen, E., "The Efficiency of High-Order Temporal Schemes," AIAA Paper 2003-0086.

[4]Carpenter, M. H. and Vatsa, V., "Higher Order Temporal Schemes with Error Controllers for Unsteady Navier-Stokes Equations," *17th AIAA*

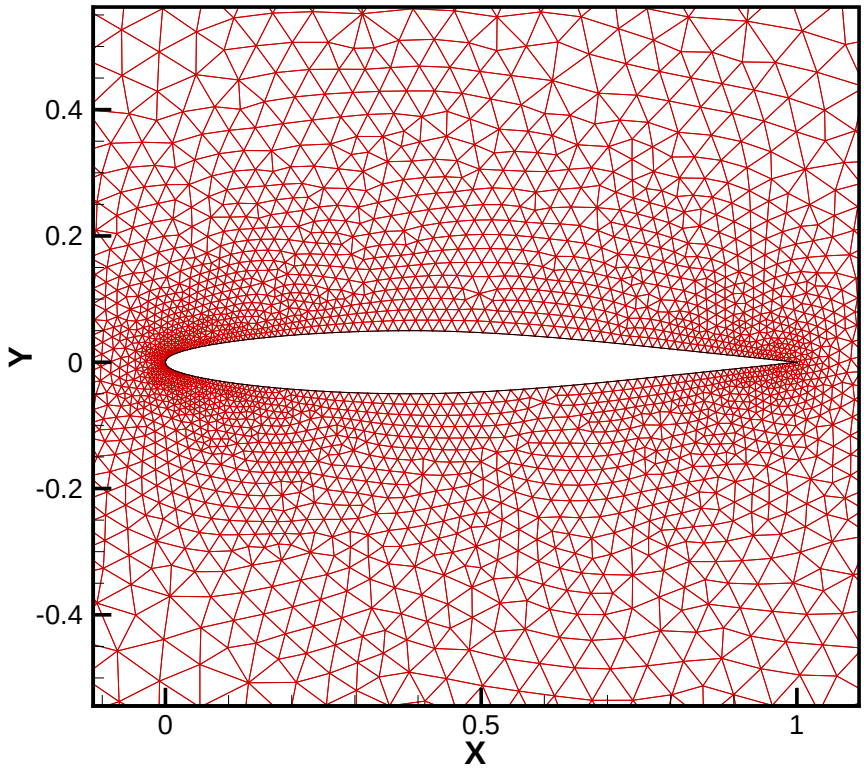

Figure 6. Computational mesh consisting of 6601 elements used in Case 1.

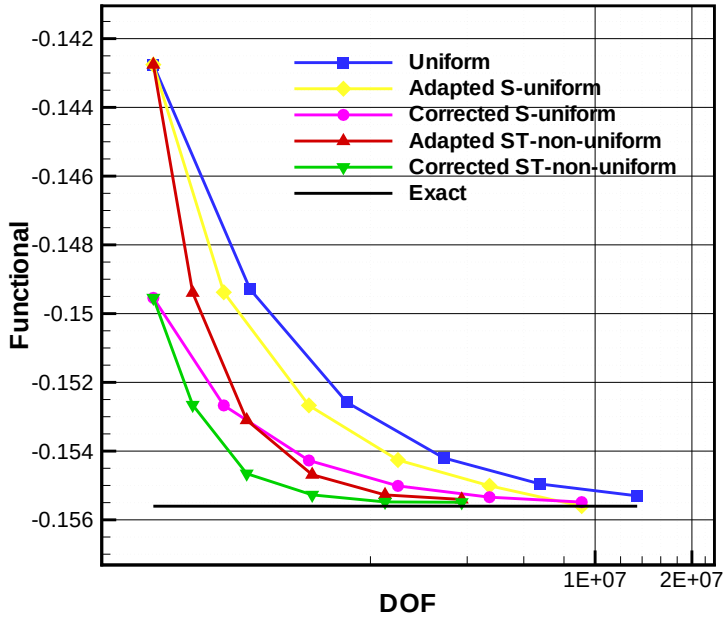

(a) Functional convergence

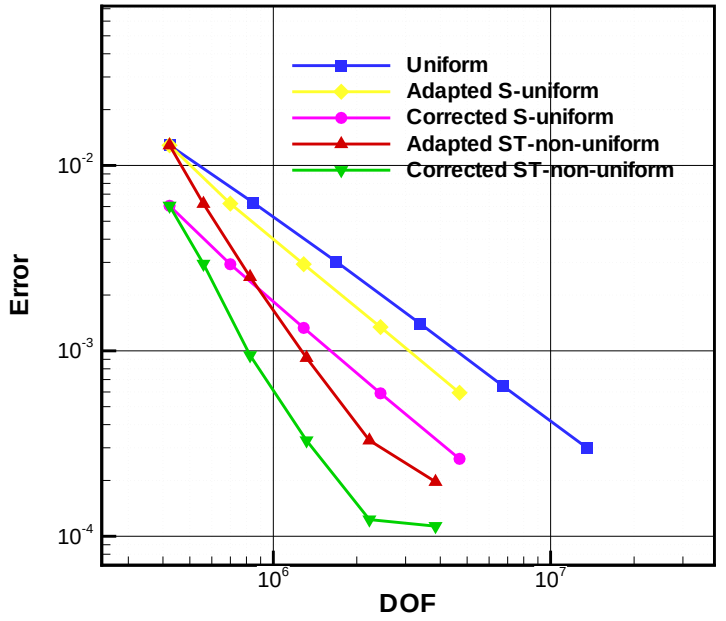

(b) Functional error convergence

Figure 7. Convergence of the functional and error in the functional with respect to total degrees-of-freedom for Case 1.

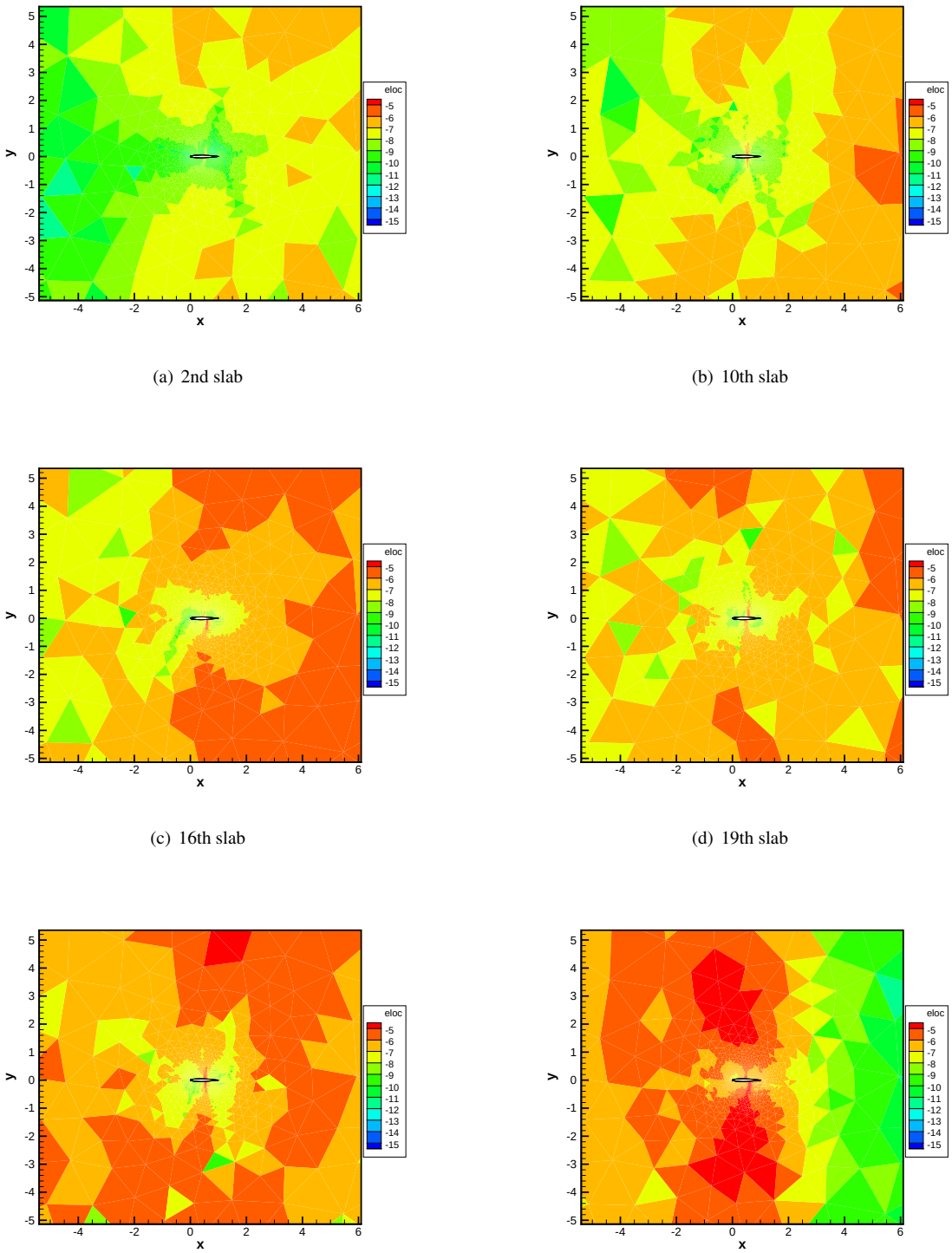

(a) 2nd slab

(b) 10th slab

(c) 16th slab

(d) 19th slab

(e) 26th slab

(f) 32nd slab

Figure 8. Initial distribution of functional relevant temporal error in space before adaptation within various time slabs for Case 1.

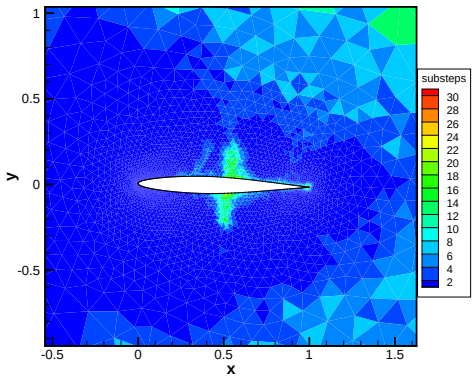

(a) 2nd slab

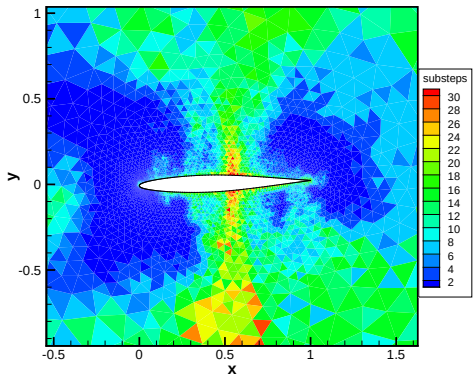

(b) 10th slab

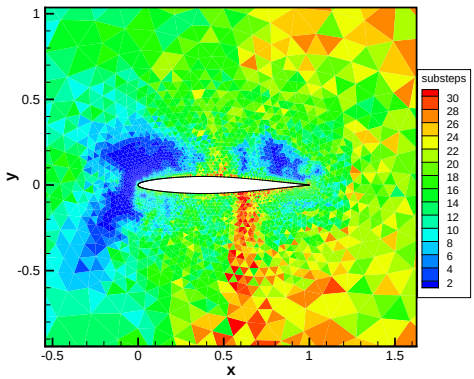

(c) 16th slab

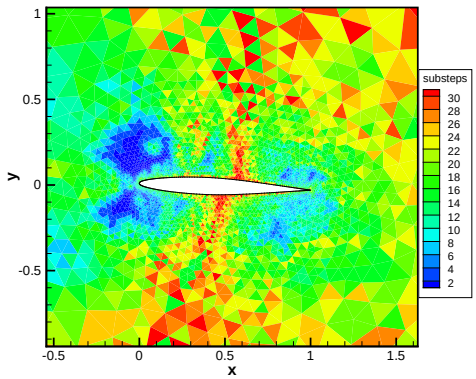

(d) 19th slab

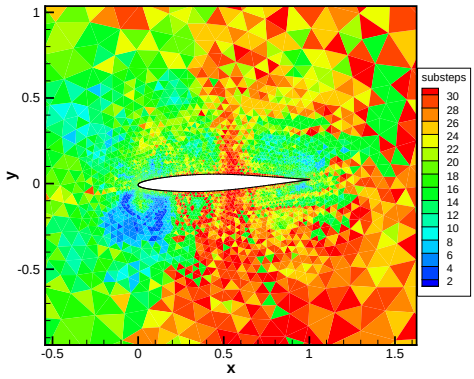

(e) 26th slab

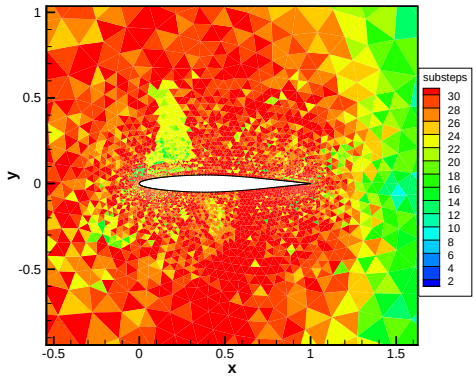

(f) 32nd slab

Figure 9. Distribution of adapted temporal resolution in spatial regions in the vicinity of the airfoil after final adaptation within various time slabs for Case 1.

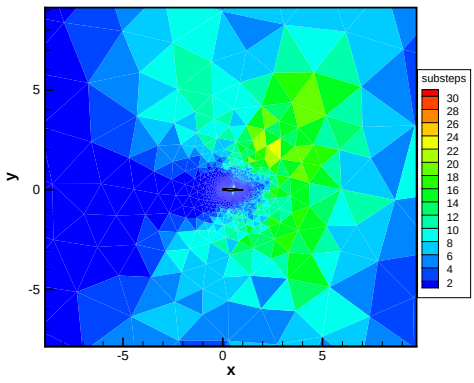

(a) 2nd slab

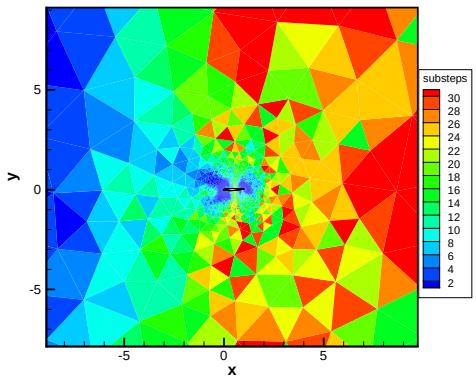

(b) 10th slab

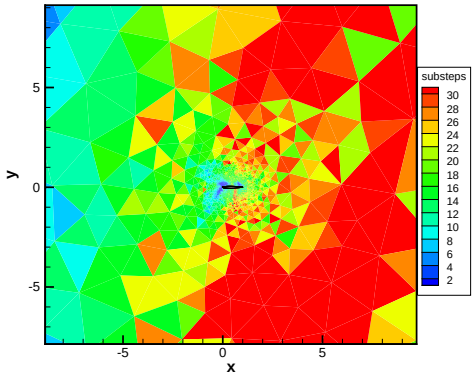

(c) 16th slab

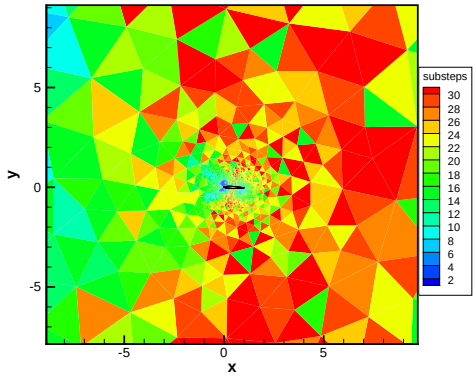

(d) 19th slab

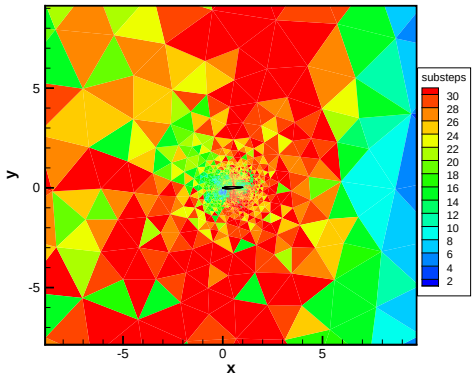

(e) 26th slab

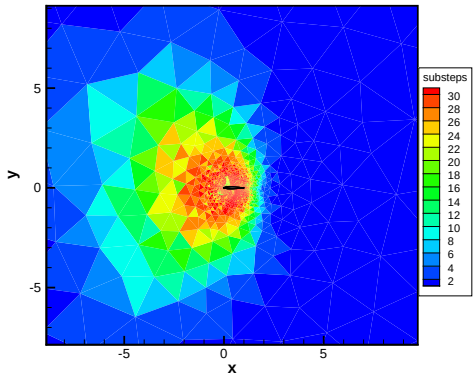

(f) 32nd slab

Figure 10. Distribution of adapted temporal resolution in space after final adaptation within various slabs for Case 1.

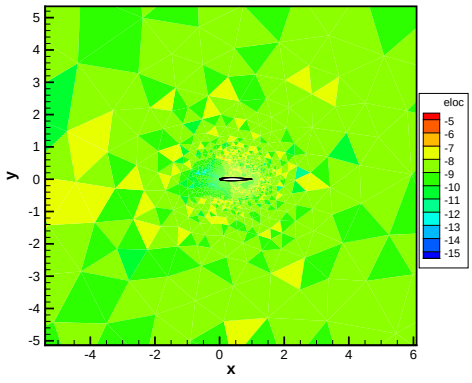

(a) Functional convergence

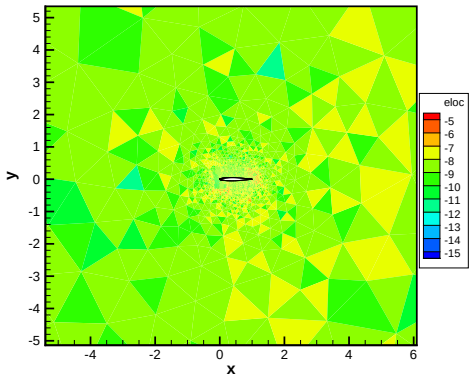

(b) Functional convergence

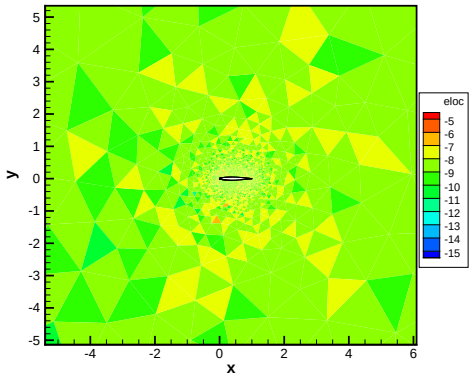

(c) Functional convergence

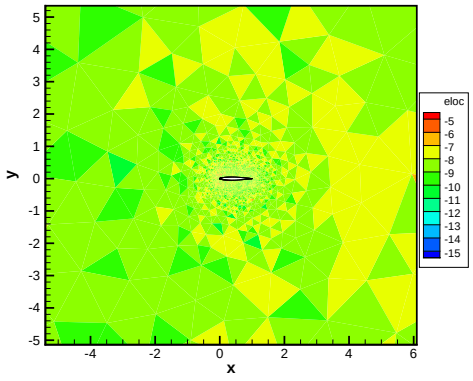

(d) Functional convergence

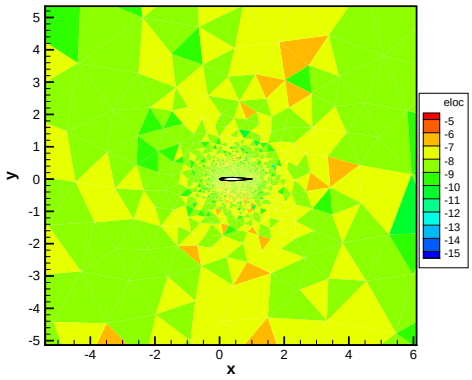

(e) Functional convergence

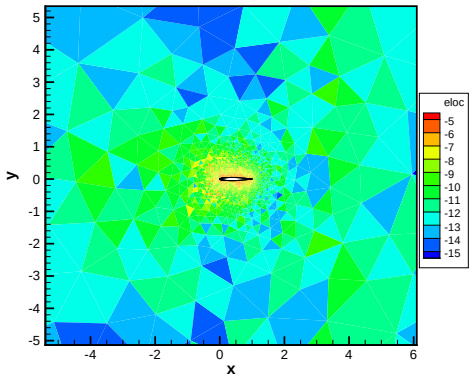

(f) Functional convergence

Figure 11. Distribution of functional relevant temporal error in space after final adaptation within various time slabs for Case 1

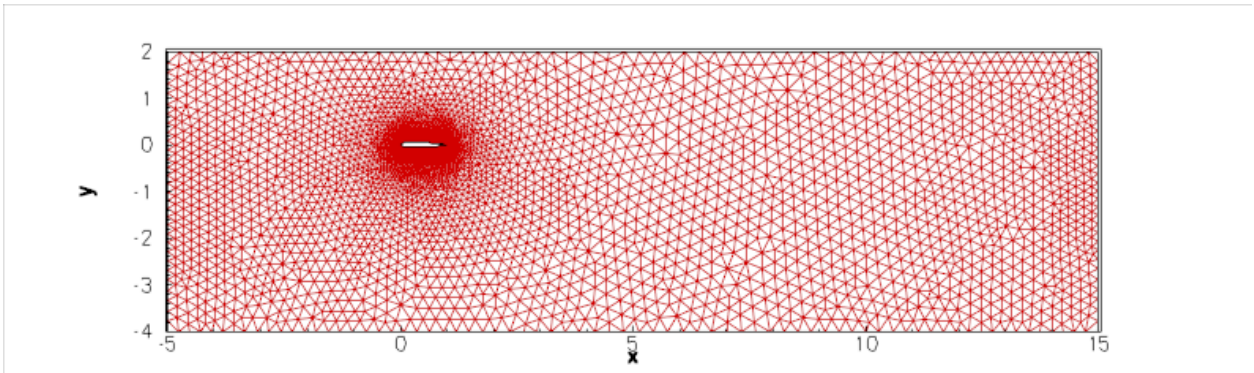

Figure 12. Computational mesh consisting of 8600 elements used in Case 2.

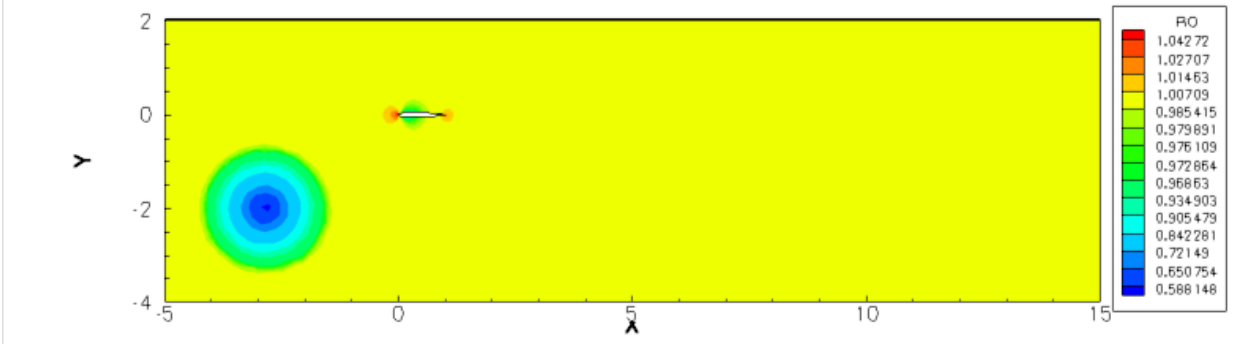

Figure 13. Density contours of initial condition for Case 2.

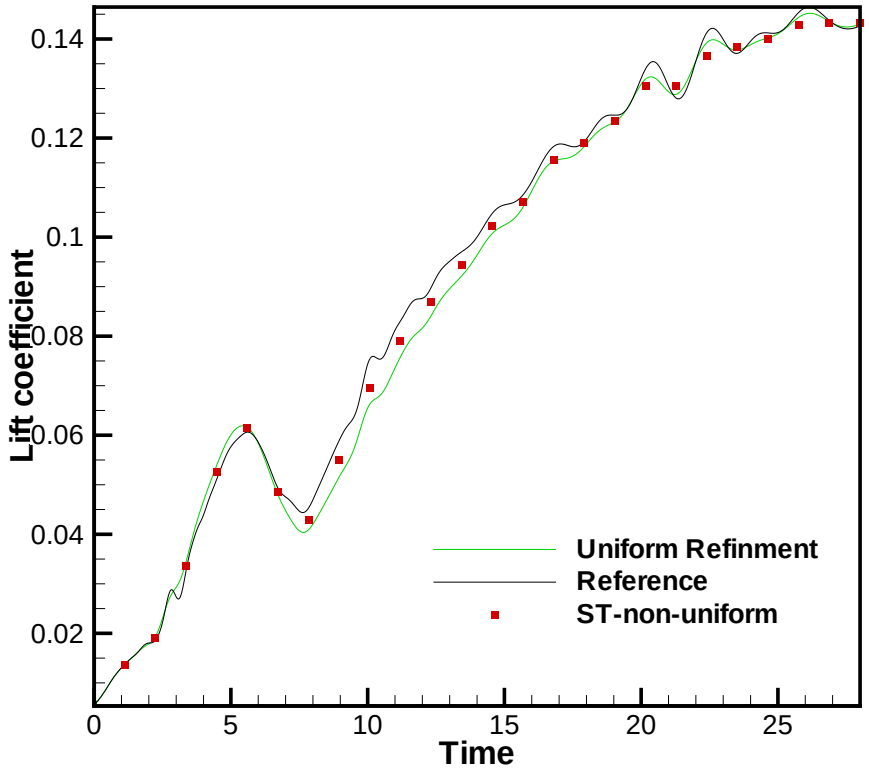

Figure 14. Variation of the lift coefficient of the airfoil in time for Case 2.

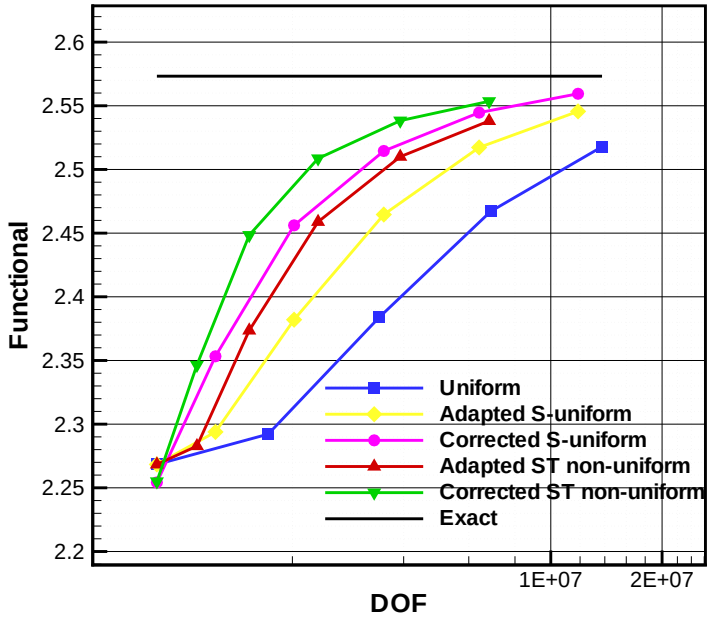

(a) Functional convergence

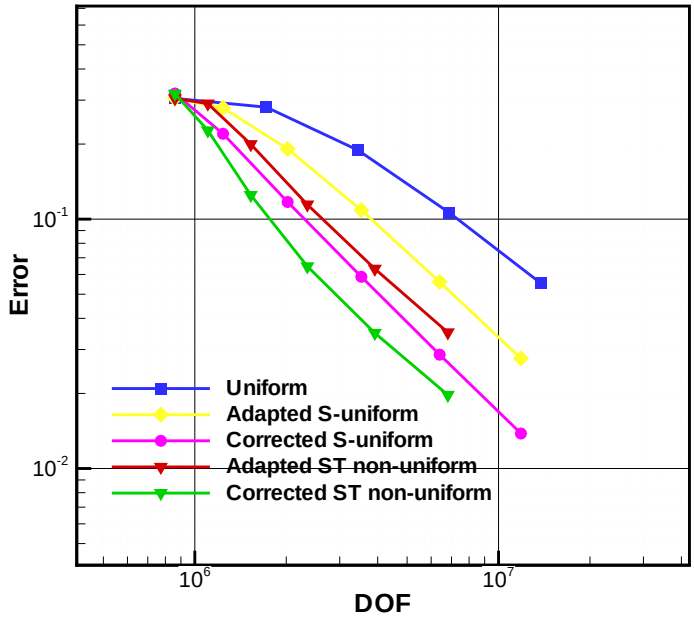

(b) Functional error convergence

Figure 15. Convergence of the functional and the error in the functional with respect to the total degrees-of-freedom for Case 2.

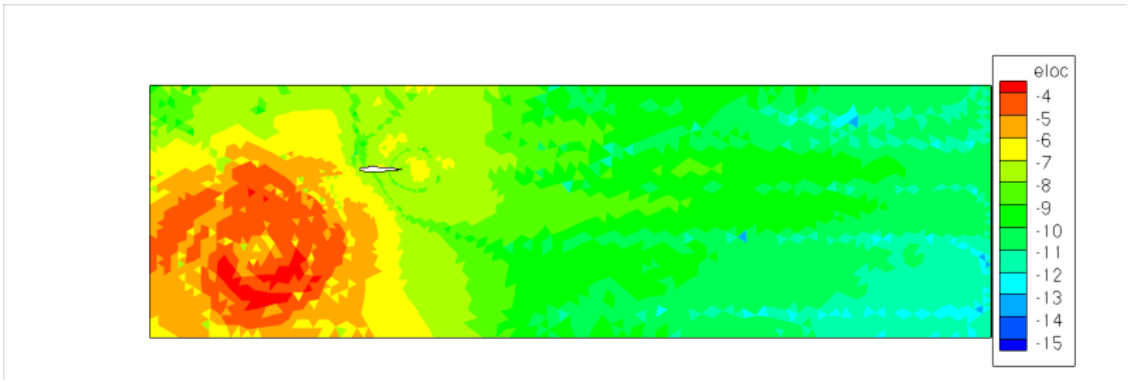

(a) 1st slab

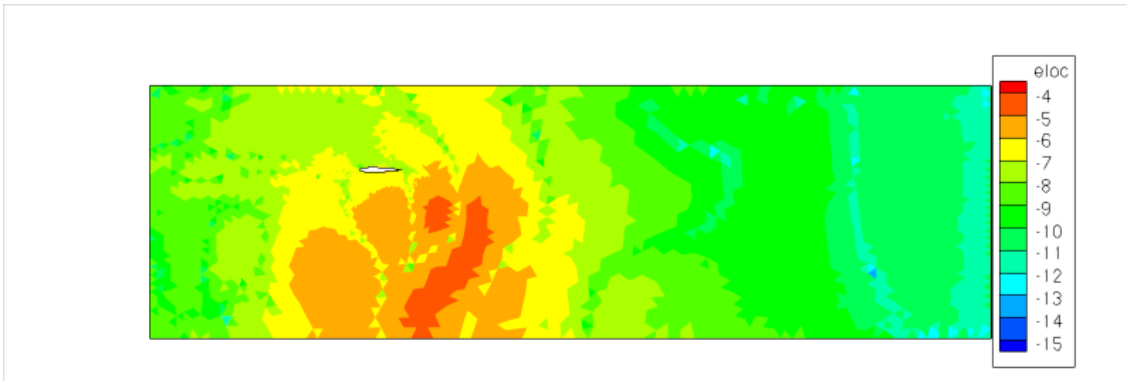

(b) 8th slab

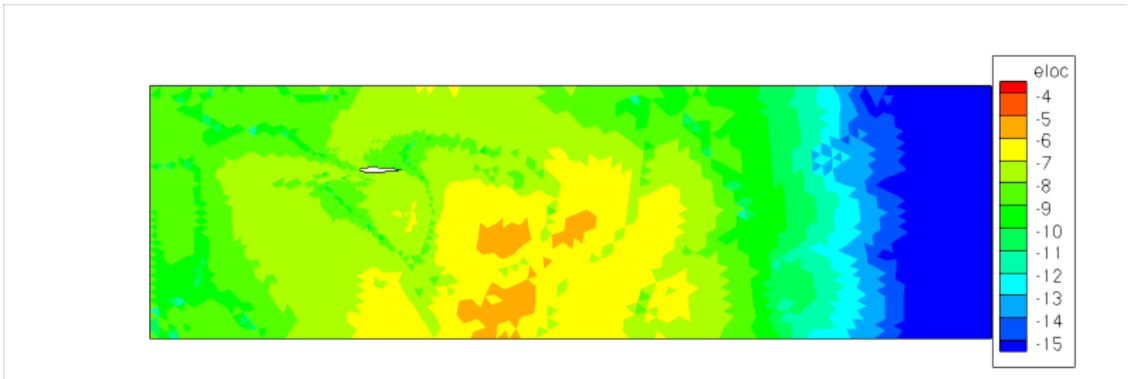

(c) 15th slab

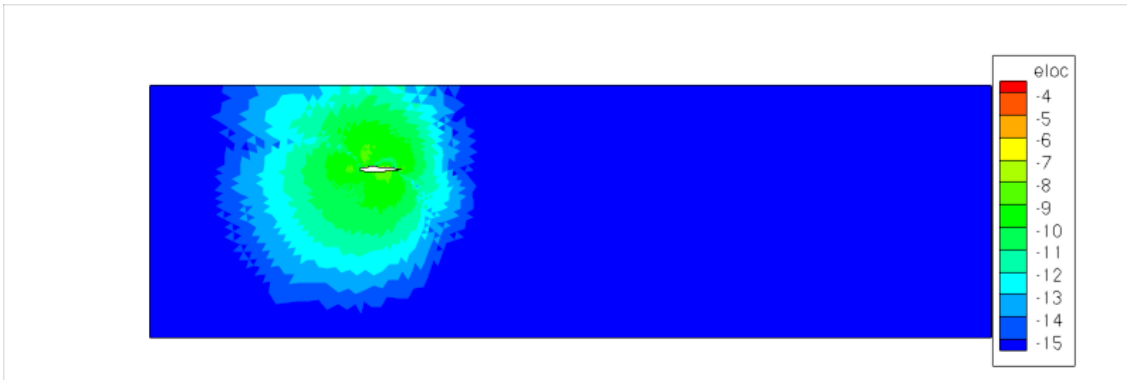

(d) 25th slab

Figure 16. Initial distribution of functional relevant temporal error before adaptation within various time slabs for Case 2.

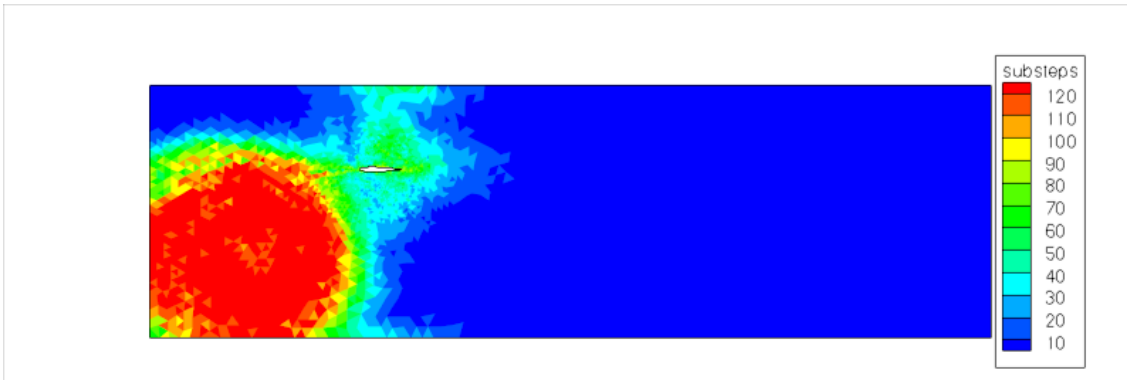

(a) 1st slab

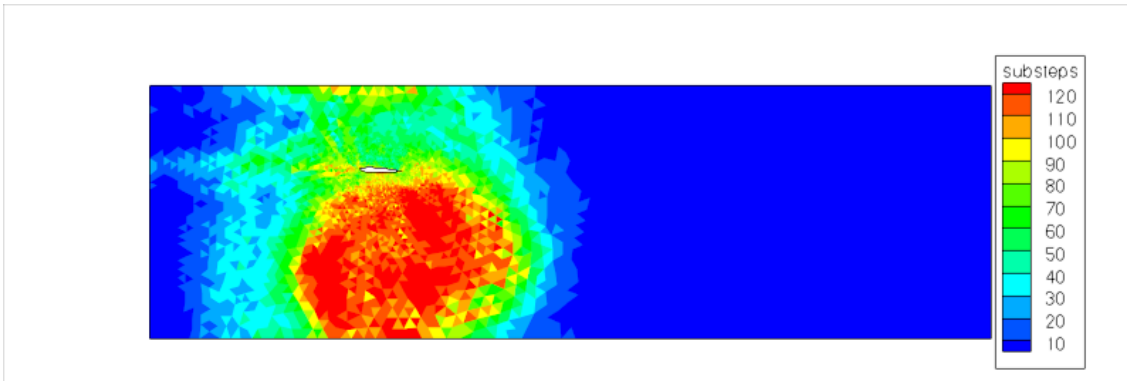

(b) 8th slab

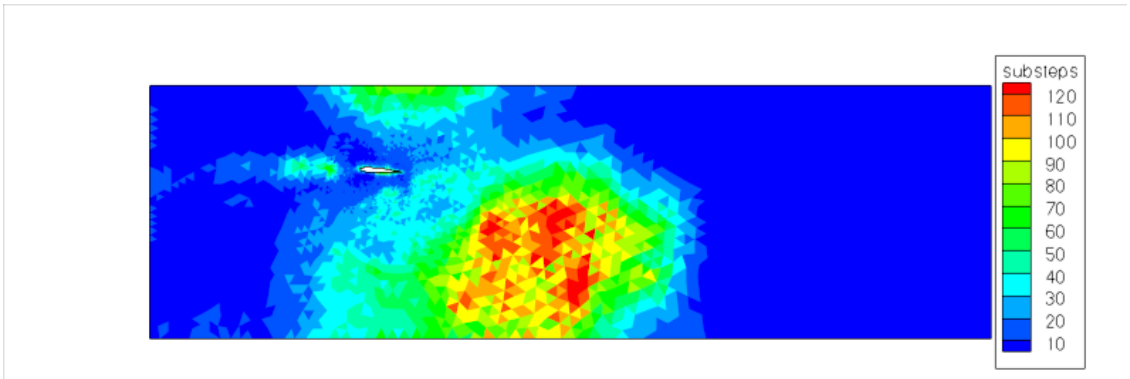

(c) 15th slab

(d) 25th slab

Figure 17. Distribution of adapted temporal resolution in space within various time slabs for Case 2.

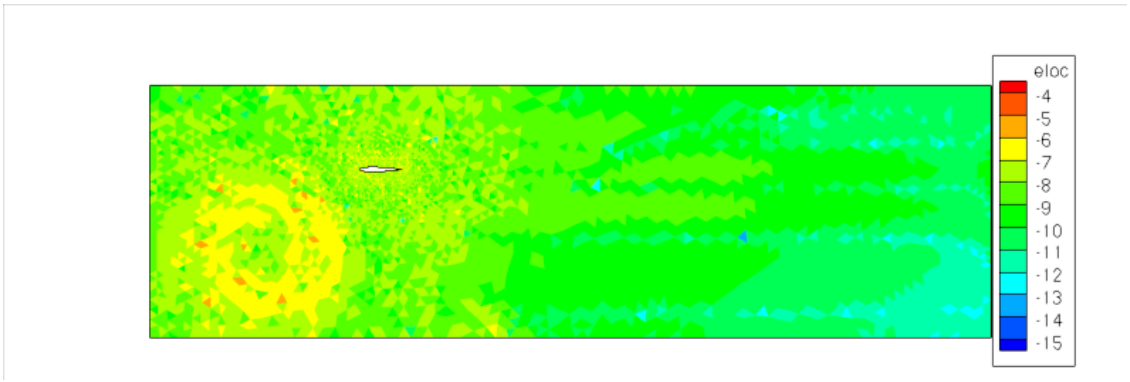

(a) 1st slab

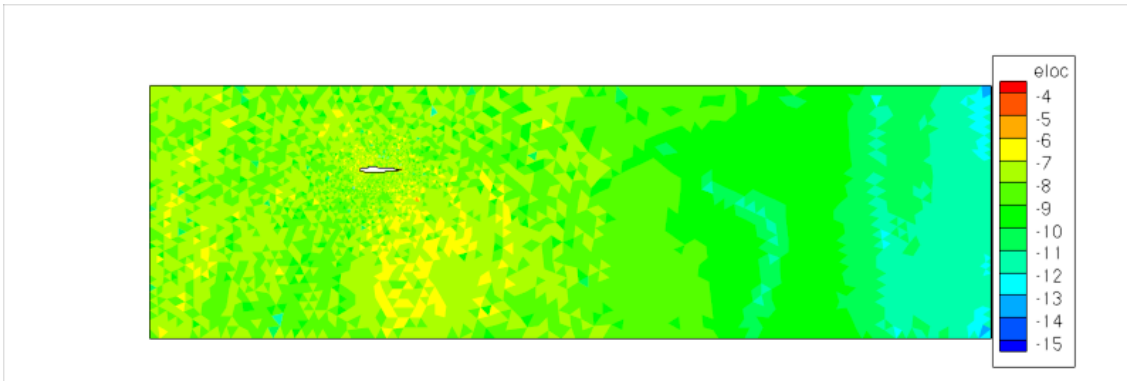

(b) 8th slab

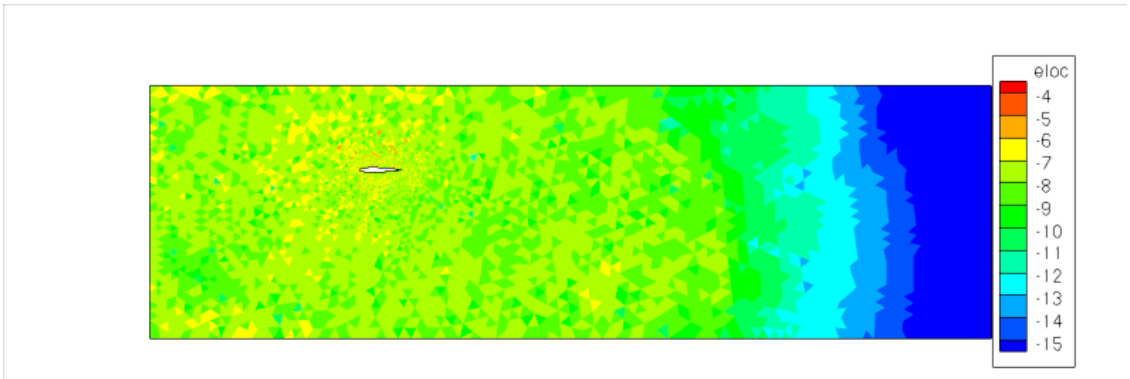

(c) 15th slab

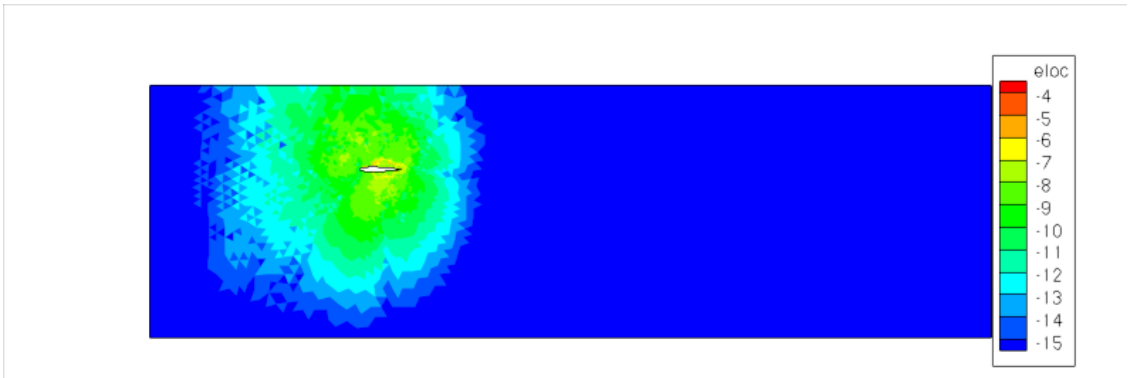

(d) 25th slab

Figure 18. Distribution of functional relevant temporal error after final adaptation within various time slabs for Case 2.

Computational Fluid Dynamics Conference, Toronta, Ontario, Canada, June 2005, 2005, AIAA Paper 2005–5245.

[5]Bijl, H., Carpenter, M., Vatsa, V., and Kennedy, C., "Implicit Time Integration Schemes for the Unsteady Compressible Navier-Stokes Equations - Laminar Flow," *Journal of Computational Physics*, Vol. 179-1, 2002, pp. 313–329.

[6]Mavriplis, D. and Yang, Z., "Construction of the discrete geometric conservation law for high-order time-accurate simulations on dynamic meshes," *Journal of Computational Physics*, Vol. 213, 2006, pp. 557–573.

[7]Yang, Z. and Mavriplis, D. J., "Higher-Order Time Integration Schemes for Aeroelastic Applications on Unstructured Meshes," *AIAA Journal*, Vol. 45-1, January 2007, pp. 138–150.

[8]Nadarajah, S., McMullen, M., and Jameson, A., "Non-Linear Frequency Domain Based Optimum Shape Design for Unsteady Three-Dimensional Flow," *Proceedings of the 44th Aerospace Sciences Meeting and Exhibit, Reno NV*, 2006, AIAA Paper 2006–387.

[9]Nadarajah, S., McMullen, M., and Jameson, A., "Optimal Control of Unsteady Flows Using Time Accuraate and Non-Linear Frequency Domain Methods," *33rd AIAA Fluid Dynamics Conference and Exhibit, Orlando, FL, June 23-26,*, 2003, AIAA Paper 2003–3875.

[10]Jameson, A., "Acceleration of Transonic Potential Flow Calculations on Arbitrary Meshes by the Multiple Grid Method," *Fourth AIAA Computational Fluid Dynamics Conference, Williamsburg, VA*, 1979, AIAA Paper 79–1458.

[11]Mavriplis, D., "Multigrid Techniques for Unstructured Meshes," *Notes prepared for 26th Computational Fluid Dynamics Lecture Series Program of the von Karman Institute of Fluid Dynamics, Rhode St Genese, Belgium*, 1995.

[12]Melson, N. D., Sanetrik, M. D., and Atkins, H. L., "Time-accurate Navier-Stokes calculations with multigrid acceleration," *6th Copper Mountain Conf. on Multigrid Methods*, 1993, pp. 423–439, NASA Conference Publication 3224.

[13]Butcher, J. C., *Numerical methods for ordinary differential equations*, Wiley, Chicester, UK, 2003.

[14]Lambert, J. D., *Numerical methods for ordinary differential systems*, Wiley, Chicester, UK, 1991.

[15]Mani, K. and Mavriplis, D. J., "Discrete Adjoint based Time-Step Adaptation and Error Reduction Unsteady Flow Problems," *18th AIAA Computational Fluid Dynamics Conference , Miami FL*, 2007, AIAA Paper 2007–3944.

[16]Mani, K. and Mavriplis, D. J., "Error Estimation and Adaptation for Functional Outputs in Time-Dependent Flow Problems," *47th AIAA Aerospace Sciences Meeting including The New Horizons Forum and Aerospace Exposition, Orlando, Florida, Jan. 5-8, 2009*, 2009, AIAA Paper 2009–1495.

[17]van der Vegt, J. J. W. and van der Ven, H., "Space–time discontinuous Galerkin finite element method with dynamic grid motion for inviscid compressible flows: I. general formulation," *Journal of Computational Physics*, Vol. 182-2, 2002, pp. 546–585.

[18]Abedi, R., Chung, S.-H., Erickson, J., Fan, Y., Garland, M., Guoy, D., Haber, R., Sullivan, J. M., Thite, S., and Zhou, Y., "Spacetime meshing with adaptive refinement and coarsening," *Annual Symposium on Computational Geometry, Proceedings of the twentieth annual symposium on Computational geometry Brooklyn, New York, USA*, 2004.

[19]Barth, T. J., "Space-Time Error Representation and Estimation in Navier-Stokes Calculations," *Lecture Notes in Computational Science and Engineering*, Vol. 56, 2007.

[20]Mavriplis, D. J., "Unstructured-Mesh Discretizations and Solvers for Computational Aerodynamics," *AIAA Journal*, Vol. 46-6, June 2008, pp. 1281–1298.

[21]Batina, J. T., "Unsteady Euler Airfoil Solutions Using Unstructured Dynamic Meshes," *AIAA Journal*, Vol. 28-8, August 1990, pp. 1381–1388.

[22]Mavriplis, D. J., "Multigrid Solution of the Discrete Adjoint for Optimization Problems on Unstructured Meshes," *AIAA Journal*, Vol. 44-1, January 2006, pp. 42–50.

[23]Saad, Y., *Iterative Methods for Sparse Linear Systems, Second Edition*, Society for Industrial and Applied Mathematics, 2003.

[24]Mani, K. and Mavriplis, D. J., "Unsteady Discrete Adjoint Formulation for Two-Dimensional Flow Problems with Deforming Meshes," *AIAA Journal*, Vol. 46-6, June 2008, pp. 1351–1364.